A Variational Method for Analyzing Vortex Flows in Radar-Scanned Tornadic Mesocyclones. Part IV: Applications to the 20 May 2013 Oklahoma Tornadic Mesocyclone

QIN XU,[a] LI WEI,[b] AND KANG NAI[a,b]

[a] *NOAA/OAR/National Severe Storms Laboratory, Norman, Oklahoma*
[b] *Cooperative Institute for Severe and High-Impact Weather Research and Operations, University of Oklahoma, Norman, Oklahoma*

(Manuscript received 15 September 2021, in final form 6 February 2022)

ABSTRACT: The variational method for vortex flow (VF) analyses, called VF-Var (formulated in Part I), is applied to the 20 May 2013 Newcastle–Moore tornadic mesocyclone observed from the operational KTLX radar and an experimental phased-array radar. The dual-Doppler-analyzed VF field reveals the following features: The axisymmetric part of the VF is a well-defined slantwise two-cell vortex in which the maximum tangential velocity is nearly 40 m s^{-1} at the edge of the vortex core (0.6 km from the vortex center), the central downdraft velocity reaches −35 m s^{-1} at 3-km height, and the surrounding-updraft velocity reaches 26 m s^{-1} at 5-km height. The total VF field is a loosely defined slantwise two-cell vortex consisting of a nearly axisymmetric vortex core (in which the ground-relative surface wind speed reaches 50 m s^{-1} on the southeast edge), a strong nonaxisymmetric slantwise downdraft in the vortex core, and a main updraft in a banana-shaped area southeast of the vortex core, which extends slantwise upward and spirals cyclonically around the vortex core. The single-Doppler analysis with observations from the KTLX radar only exhibits roughly the same features as the dual-Doppler analysis but contains spurious vertical-motion structures in and around the vortex core. Analysis errors are assessed by leveraging the findings from Parts II and III, which indicate that the dual-Doppler-analyzed VF is accurate enough to represent the true VF but the single-Doppler-analyzed VF is not (especially for nonaxisymmetric vertical motions in and around the vortex core), so the dual-Doppler-analyzed VF should be useful for initializing/verifying high-resolution tornado simulations.

SIGNIFICANCE STATEMENT: After the variational method for vortex flow (VF) analyses, called VF-Var (formulated in Part I of this paper series), was tested successfully with simulated radar observations in Part II and its sensitivity to vortex center location error was examined in Part III, the method is now applied to the 20 May 2013 Newcastle–Moore tornadic mesocyclone observed from the operational KTLX radar and an experimental phased-array radar. Analysis errors are assessed by leveraging the findings from Parts II and III. The results indicate that the dual-Doppler-analyzed VF is accurate enough to represent the true VF (although the single-Doppler-analyzed VF is not especially for nonaxisymmetric vertical motions in and around the vortex core) and thus should be useful for initializing/verifying high-resolution tornado simulations.

KEYWORDS: Mesocyclones; Tornadoes; Vortices; Radars/Radar observations; Variational analysis

1. Introduction

Three-dimensional (3D) and 3.5D variational methods were developed at the National Severe Storms Laboratory for analyzing storm winds from radar observations (Gao et al. 2013; Xu et al. 2010, 2015a). These methods can resolve storm-scale wind fields to certain extents, but they all have an intrinsic limitation to resolve vortex flow (VF) fields in tornadic mesocyclones due to the absence of VF-dependence in the background error covariance. To overcome this limitation, VF-dependent background error covariance functions were formulated first in 2D (Xu et al. 2015b) for analyzing VFs from radar low-elevation scans of tornadic mesocyclones and then extended to 3D in a variational method, called VF-Var (Xu 2021, hereafter Part I), for analyzing 3D VFs with the vortex center described and estimated as a continuous function of height and time by using a three-step method (Xu et al. 2017). In this VF-Var, the local Cartesian coordinate system is transformed into a slantwise moving cylindrical coordinate system cocentered with the estimated vortex center in the 4D space to facilitate the formulations of VF-dependent background error covariance functions and to define the analysis domain with the analysis time window determined by the radar volume scan time period. This VF-Var is able to analyze both the axisymmetric and asymmetric parts of VF in a slantwise vortex-following coordinate system, whereas other previous methods were developed for analyzing only the axisymmetric structures (Lee and Wurman 2005), parameterized structures (Potvin et al. 2011), or horizontal structures of VFs (Xu et al. 2015b) in radar-observed tornadic mesocyclones. Because of this, the VF-Var should be particularly suitable (at least, more suitable than other previous methods) for initializing/verifying high-resolution model simulations of radar-observed tornadic mesocyclones and related future data assimilation applications.

The VF-Var was tested with simulated radar radial-velocity scans of analytically formulated benchmark vortices with the vortex center location given either accurately (Xu and Wei 2021, hereafter Part II) or inaccurately (Xu and Wei 2022, hereafter Part III). The major findings from these tests are as follows: (i) When the vortex center location is accurately

Corresponding author: Qin Xu, Qin.Xu@noaa.gov

DOI: 10.1175/JAS-D-21-0247.1

estimated, the VF-Var performs very well (or reasonably well) with dual-Doppler (or single-Doppler) scans, and errors in the single-Doppler-analyzed velocities are mainly in the unobserved velocity components and only in fractions of the true velocities. (ii) When the vortex center location is estimated inaccurately with an error up to a half of vortex core radius, the dual-Doppler-analyzed VF still can have adequate accuracies outside the vortex core, and single-Doppler-analyzed VF can be adequately accurate mainly for the observed velocity component outside the vortex core. As a follow-up of Part II and Part III, this paper further tests the VF-Var by performing dual-Doppler and single-Doppler analyses with real radial velocities scanned from the operational KTLX radar and the National Weather Radar Testbed experimental phased-array radar (PAR) (Zrnić et al. 2007; Heinselman and Torres 2011) for the 20 May 2013 Newcastle–Moore tornadic mesocyclone in Oklahoma, while the findings from Part II and Part III can be leveraged to assess the analysis errors. The VF-Var can be performed either in a single step or in two steps (see the algorithm flowcharts in Fig. 4 of Part I). Since these two approaches have similar performances for the applications considered in this paper but the two-step approach is computationally much more efficient than the single-step approach [see summary (v) in the conclusion section of Part II], this paper will present applications of VF-Var only with the two-step approach. The results obtained in this paper should be useful for initializing/verifying high-resolution model simulations of this particular tornadic mesocyclone.

The paper is organized as follows: Section 2 describes radar radial-velocity observations and estimates the vortex center location. Section 3 estimates/specifies the parameter values for the VF-dependent background error covariance functions formulated in the VF-Var. Sections 4 and 5 apply the VF-Var to the dual-Doppler velocity observations (from KTLX and PAR) and single-Doppler velocity observations (from KTLX only), respectively, for the 20 May 2013 Oklahoma tornadic mesocyclone. Section 6 assesses the accuracies of the dual-Doppler and single-Doppler-analyzed VFs. Section 7 highlights the results presented in appendix B in which the VF-Var is applied to additional dual-Doppler velocity observations. Conclusions follow in section 8.

2. Radar radial-velocity observations and estimation of vortex center location

In the afternoon of 20 May 2013, a tornado began northwest of Newcastle, Oklahoma, and quickly increased to an EF5-rated tornado before it struck Moore, Oklahoma. This EF5 tornado moved initially northeastward and then east-northeastward through Moore, eventually dissipating in a rural area east of Moore at 2035 UTC (Burgess et al. 2014; also see the tornado track shown by the solid dark purple line in Fig. B1 of this paper). A brief overview of this tornado can be found in Snook et al. (2019). This EF5 tornado and its parent mesocyclone were well observed by the KTLX radar and the PAR. Figures 1a and 1b (or Fig. 1c and 1d) show the images of reflectivity and dealiased radial velocity from KTLX on 0.5° tilt at 2004:28 UTC (or PAR on 0.5° tilt at 2004:40 UTC), respectively. The tornado vortex center, estimated as a by-product of the mesocyclone-targeted dealiasing method (Xu and Nai 2017), is marked by the yellow dot in each panel of Fig. 1. As shown the vortex center was located about 28 km west of the KTLX radar site at 2004:28 UTC and about 14 km northwest of the PAR site at 2004:40 UTC.

The VF-Var is applied to radial velocities observed from the KTLX radar and the PAR for the aforementioned tornadic mesocyclone after these observed radial velocities are thoroughly dealiased (Xu and Nai 2017). One volume of dealiased radial velocities scanned from KTLX on 14 tilts (at 0.5°, 0.9°, 1.3°, 1.8°, 2.4°, 3.1°, 4.0°, 5.1°, 6.4°, 8.0°, 10.0°, 12.5°, 15.6°, and 19.5°) over the time period from 2004:28 to 2007:50 UTC are used for the single-Doppler analysis in section 5, and one sector volume of dealiased radial velocities from PAR on 10 tilts (at 0.5°, 0.9°, 1.3°, 1.8°, 2.4°, 3.1°, 4.0°, 6.4°, 8.0°, and 10.0°) over the time period from 2004:40 to 2005:24 UTC are used in addition to the one volume from KTLX for the dual-Doppler analysis in section 4. The range gate spacing is 0.25 km in the radial direction for both KTLX and PAR scans, and the beam spacing in the azimuthal direction is 0.5° for KTLX and 1° for PAR scans. The analysis time window is set to 4 min, from 2003:50 to 2007:50 UTC, to cover the aforementioned time periods of KTLX and PAR scans, that is, between $0 \le t \le 4$ min with $t = 0$ corresponding to 2003:50 UTC.

The three-step method of Xu et al. (2017) is used to estimate the vortex center location, $\mathbf{x}_c \equiv (x_c, y_c)$ as a smooth vector function of (z, t), from radar observed mesocyclones. In this three-step method, the vortex center location is estimated on each radar scan tilt as a by-product of the mesocyclone-targeted dealiasing (Xu and Nai 2017) in the first step, so a discrete dataset of vortex center locations is generated at irregularly distributed points in the two-dimensional space of (z, t). The ith vortex center location in this discrete dataset is denoted by $\mathbf{x}_{ci}$, which is at the ith discrete point, denoted by (z_i, t_i), in (z, t). In Xu et al. (2017), the three-step method was applied to 10 and 22 consecutive volumes of dealiased radial velocities from the KTLX radar and PAR, respectively, over the time period of 42.03 min from 1951:42 to 2033:44 UTC 20 May 2013, but $\mathbf{x}_c(z, t)$ was estimated only up to $z = 4$ km due to the lack of $\mathbf{x}_{ci}$ (in the discrete dataset) above 4 km over the 42.03 min period. Over the 4 min analysis time window considered in this paper, however, the vortex was detected with $\mathbf{x}_{ci}$ estimated above $z = 4$ km (and up to about 8 km) from KTLX scans. On the other hand, $\mathbf{x}_{ci}$ estimated from PAR scans were all below 4 km, and radial velocities scanned from PAR were all below 5.5 km and mostly below 5 km. The analysis domain height is thus set to 5 km, and $\mathbf{x}_c(z, t)$ is reestimated up to $z = 5$ km using $\mathbf{x}_{ci}$ from both KTLX and PAR.

The two components of estimated $\mathbf{x}_c(z, t)$ are plotted for $0 \le z \le 5$ km over the analysis time window in Figs. 2a and 2b, where the black (or green) plus signs mark the 11 (or 10) discrete points (z_i, t_i) at which the discrete vortex center locations $\mathbf{x}_{ci}$ are estimated from the one volume KTLX scan (or one sector-volume PAR scan). The horizontal moving velocity of the vortex center, $\mathbf{u}_c \equiv \partial_t \mathbf{x}_c$, is also estimated as a smooth

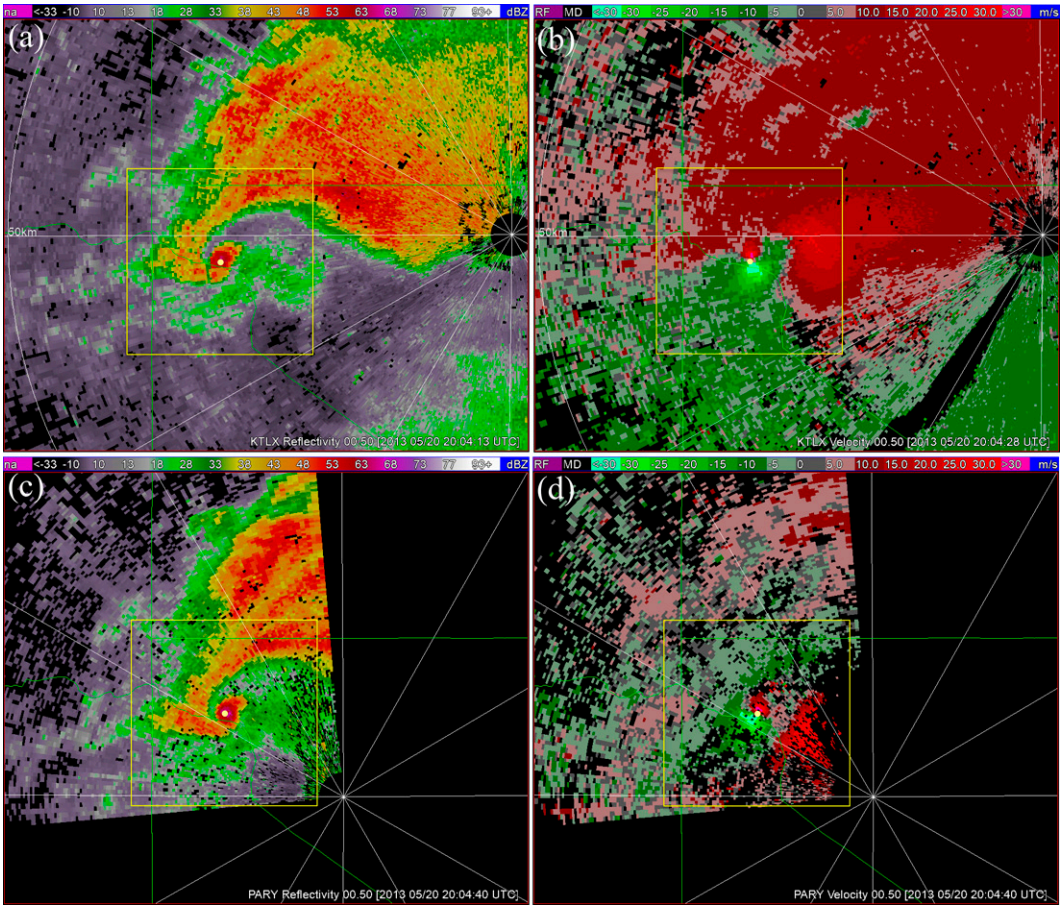

FIG. 1. Images of (a) reflectivity and (b) dealiased radial velocity from KTLX at 0.5° tilt at 2004:28 UTC. Images of (c) reflectivity and (d) dealiased radial velocity from PAR at 0.5° tilt at 2004:40 UTC. In each panel, the yellow dot marks the estimated vortex center and the analysis domain is shown by the square area of 20×20 km^2 enclosed by the thin yellow boundary line.

vector function of (z, t); the two components of estimated $\mathbf{u}_c(z, t)$ are plotted for $0 \le z \le 5$ km over the analysis time window in Figs. 2c and 2d. The estimated $\mathbf{x}_c(z, t)$ and $\mathbf{u}_c(z, t)$ are used for the coordinate transformation and associated operator transformation [see (2.1) and (3.1)].

Figure 3 shows a 3D perspective of the estimated vortex center axis viewed in the local Cartesian coordinate system (x, y, z) at five different times, 1 min apart, from the beginning to the end of the analysis time window, where the origin of (x, y, z) is at $\mathbf{x}_c(0, 0)$, that is, the estimated vortex center location at $(z, t) = (0, 0)$, and the vortex center axis is a continuous vector function of z defined by $\mathbf{x}_c(z, t)$ at given t. As shown, during the 4 min of the analysis time window, the vortex center axis becomes less slanted and more upright below $z = 3$ km as it moves eastward and slightly northward. This vortex center axis is taken to be the slantwise vertical coordinate axis for z' in the vortex-following coordinate system (x', y', z', t') defined by

$$(x', y', z', t') \equiv (x - x_c, y - y_c, z, t) \tag{2.1}$$

as in (2.1) of Part I.

The analysis domain is confined by $|x'| \le 10$ km, $|y'| \le 10$ km, and $0 \le z' \le 5$ km in the vortex-following coordinate system (x', y', z', t') with $t' = t$ confined by $0 \le t' \le 4$ min (i.e., between 2003:50 and 2007:50 UTC) within the analysis time window. In (x, y, z, t), the analysis domain is a moving and time-varying slantwise cubic box. In the vortex-following coordinate system, the KTLX antenna location moves horizontally from $(x', y') = (27.834, 2.778)$ to $(25.816, 2.260)$ km and the PAR antenna location moves horizontally from $(x', y') = (11.510, -7.712)$ to $(9.679, -8.231)$ km during the 4 min of the analysis time window. The one volume of radial-velocity data from KTLX and one sector volume of radial-velocity data from PAR are transformed from their respective radar coordinate systems into the local Cartesian coordinate system, and then into the vortex-following coordinate system by neglecting small time differences (<10 or 20 s) between radial-velocity data collected along radar beams in different azimuthal directions but on the same tilt of radar scans. However, time differences (≈20 s for KTLX radar) between radial-velocity data collected on different tilts of radar scans are not neglected, so data points on each tilt of radar scans are transformed into (x', y', z', t') corresponding to each value of t' and

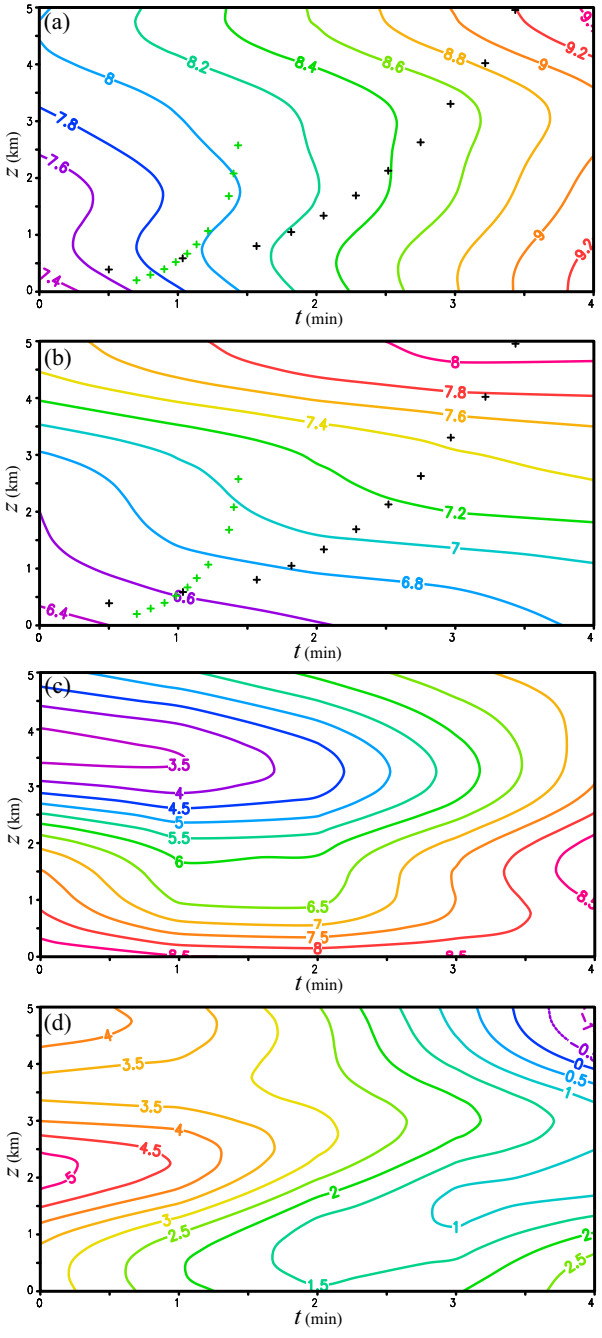

FIG. 2. (a) $x_c(z, t)$ and (b) $y_c(z, t)$ plotted by color contours every 0.2 km, and (c) $u_c(z, t)$ and (d) $v_c(z, t)$ plotted with color contours every 0.5 m s^{-1} for $0 \le z \le 5$ km over the analysis time window confined by $0 \le t \le 4$ min with $t = 0$ corresponding to 2003:50 UTC. The black (or green) plus signs in (a) and (b) mark the 11 (or 10) discrete points (z_i, t_i) at which the discrete vortex center locations $\mathbf{x}_{ci}$ are estimated from the one volume KTLX scan (or one sector-volume KTLX scan) within the analysis time window. The fitting residuals, denoted and defined by $(\Delta x_{ci}, \Delta y_{ci}) = \Delta\mathbf{x}_{ci} \equiv \mathbf{x}_{ci} - \mathbf{x}_c(z_i, t_i)$, are listed below: $(\Delta x_{ci}, \Delta y_{ci})$ = (−0.068, −0.148), (−0.257, 0.212), (−0.348, −0.086), (−0.311, 0.213), (−0.254, 0.194), (−0.276, 0.378), (−0.418, 0.521), (0.037, −0.184), (−0.261, −0.193), (0.001, 0.311), and (0.028, 0.073) km, respectively, at the 11 discrete points

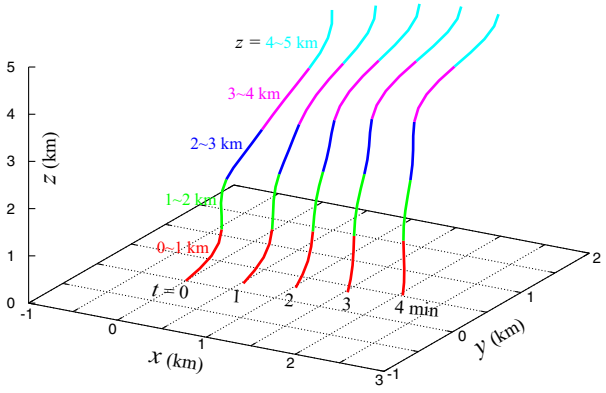

FIG. 3. 3D perspective of the estimated vortex center axis viewed in the local Cartesian coordinate system (x, y, z) at five different times, 1 min apart, from the beginning to the end of the analysis time window between $0 \le t \le 4$ min. The origin of (x, y, z) is at $\mathbf{x}_c(0, 0)$—the estimated vortex center location at $(z, t) = (0, 0)$. The five colored segments (in red, green, blue, purple, and cyan) of vortex center axis at each time indicate the estimated vortex center axis in five different vertical layers of 1-km depth from $z = 0$ to 5 km.

thus each radar antenna location in (x', y', z'). Transformed data points in and above the analysis domain are thinned (for the clarity of display only) and projected along the y' coordinate onto the vertical plan of (x', z') and then plotted cumulatively by different color symbols for different tilts of scans from KTLX (or PAR) in Fig. 4a (or Fig. 4b). As shown in Fig. 4b, data points from PAR are all below 5.5 km and mostly below 5 km. Because of this, as explained earlier, the analysis domain is confined by $0 \le z' \le 5$ km. Data points on the highest tilt (19.5°) from KTLX are all above the analysis domain and thus not plotted in Fig. 4a. The total number of radial-velocity observations from KTLX (or PAR) available/used in the analysis domain is 45 529 (or 73 842). These radial-velocity observations are assumed loosely to have spatially uncorrelated errors with their error standard division set to 2 m s^{-1} based on previous studies of radar radial-velocity observation error statistics (Xu et al. 2007a,b).

3. VF-dependent background error covariance parameter settings

It is well known in variational data analyses and assimilation (Daley 1991) that the error covariances specified for the observations and background fields in the cost-function

←

marked sequentially upward by the black plus signs as shown in (a) and (b). $(\Delta x_{ci}, \Delta y_{ci})$ = (0.262, 0.117), (0.130, 0.043), (0.070, 0.068), (0.187, 0.263), (0.113, 0.178), (0.240, −0.000), (0.139, 0.193), (−0.011, −0.053), (0.223, 0.103), and (0.255, 0.016) km, respectively, at the 10 discrete points marked sequentially upward by the green plus signs in (a) and (b). The local (x, y, z) coordinate system used here is the same as in Fig. 1 of Xu et al. (2017), but the x (or y) coordinate origin should be 60 km west of 97.6813°W (or 27 km south of 35.2482°N) [rather than just at 97.6813°W (or 35.2482°N) as inaccurately given in the caption of above cited figure].

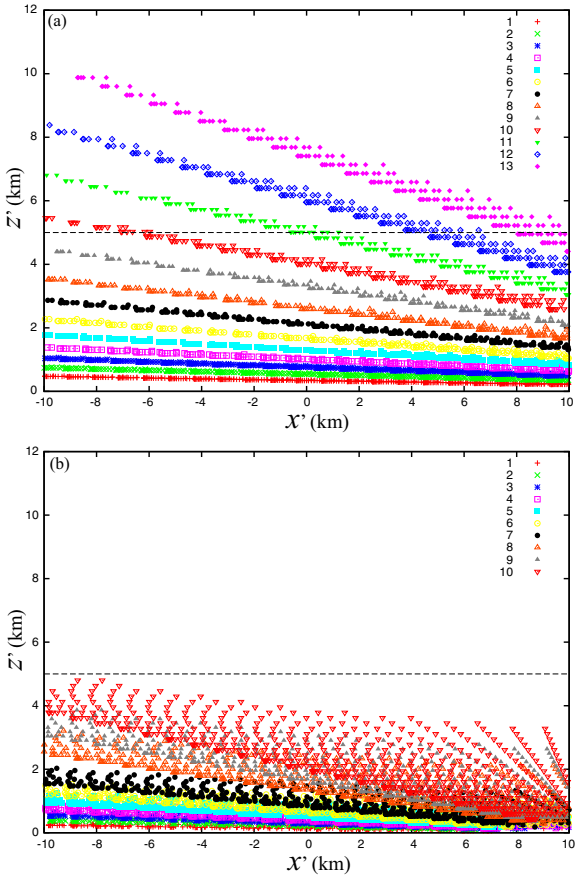

FIG. 4. (a) Thinned data points at 13 tilts of the KTLX volume scan projected along the y' coordinate onto the vertical plan (x', z') and plotted cumulatively in (x', z') by different color symbols for different tilts. (b) As in (a), but for thinned data points at 10 tilts of the PAR sector-volume scan. For clarity of display, the KTLX data points in (a) are thinned from the original every 0.25 km and 0.5° to every 2 km and 2° in the radar radial and azimuthal directions, respectively, and the PAR data points in (b) are thinned from the original every 0.25 km and 1° to every 2 km and 4° in the radar radial and azimuthal directions, respectively. The dashed horizontal line at $z' = 5$ km shows the top of the analysis domain and each type of color symbol is plotted and labeled with its associated tilt number along the vertical column on the upper right side in each panel. Note that the radial-velocity data used by the analyses are not thinned.

control the analysis outcome by controlling how observations affect the analysis increment (i.e., analyses minus background). It is thus necessary and important to properly estimate/specify these error covariances for variational data analyses. For the radial-velocity observations used in this paper, the observation error covariance has been estimated/specified in the previous section. In this section, we only need to estimate/specify the error variances and decorrelation radial lengths and depths in the VF-dependent background error covariance functions formulated in Part I.

As explained in section 2c of Part I, for the stand-alone applications considered in this paper, the background velocity is zero in (x', y', z') so the background error field is simply the true VF field (i.e., the true total wind minus $\mathbf{u}_c$), while the true VF field can be approximated by a dual-Doppler-analyzed VF field. As shown in Fig. 1 and Table 1 of Part I, the VF field is expressed in (x', y', z') by the contravariant velocity that is defined by $(u', v', w') \equiv d_t(x', y', z')$ and is related to the total velocity, (u, v, w), in the original Cartesian coordinate system (x, y, z) by

$$(u', v', w') = (u - u_c - w\partial_z x_c, v - v_c - w\partial_z y_c, w)\cdot \quad (3.1)$$

As explained in sections 3b and 4b of Part I, to facilitate the constructions of VF-dependent covariance functions, it is necessary to transform (x', y', z') first into a vortex-following slantwise cylindrical coordinate system (R, β, z') with $R \equiv (x'^2 + y'^2)^{1/2}$ and $\tan\beta \equiv y'/x'$, in which (u', v', w') can be re-expressed by (V_T, V_R, w') where V_T and V_R are the tangential and radial components of (u', v'), respectively. The radial coordinate R is then further transformed into $r \equiv \text{arsinh}(R/R_c)/l$ and the vertical coordinate z' is scaled by the decorrelation depth H [see (3.6) of Part I], where $R_c = 1.5$ km is the radial-length scale that ensures $\text{arsinh}(R/R_c) \approx R/R_c$ within the vortex core and l is the radial decorrelation length factored into r. When r is transformed back to R in the physical space, the corresponding radial decorrelation length becomes a monotonically increasing function of R given by $L = 2(R^2 + R_c^2)^{1/2}\sinh(l/2)$, which has the desired properties [such as $L \approx 2R_c\sinh(l/2) \approx R_c l$ for $R \ll R_c$ and $L \approx 2R\sinh(l/2) \approx Rl$ for $R \gg R_c$] that facilitate the constructions of VF-dependent covariance functions.

Since the background error field is simply the true VF field as explained earlier, the background error variance and associated (l, H) should and can be properly specified for each control variable in consistency with the true VF structure and intensity estimated by a dual-Doppler analysis. For the axisymmetric part of (V_T, V_R), denoted by (V_T^s, V_R^s), the tangential velocity V_T^s tends to have narrower and deeper structures than the radial velocity V_R^s (see Fig. 2 of Fiedler and Garfield 2010), and these structural features are also seen from the dual-Doppler-analyzed VF in section 4 as a proxy of the true background error field. Thus, we can set $l = l_1 = 1/2$ and $H = H_1 = 2$ km for V_T^s but set $l = l_2 = 1$ and $H = H_2 = 1$ km for the secondary circulation expressed by the cylindrical streamfunction, denoted by ψ^s and defined by $\rho_a R(V_R^s, w^s) \equiv (-\partial'_z R\psi^s, \partial_R R\psi^s)$ in (3.2) of Part I. For the above settings of $l = l_1 = 1/2$ and $l = l_2 = 1$, the corresponding radial decorrelation lengths at $R = R_c$ in the physical space are $L = L_1 = R_c/\sqrt{2} \approx 1$ km and $L = L_2 = \sqrt{2}R_c \approx 2$ km, respectively.

Furthermore, consistent with the cylindrical-volume-averaged root-mean-square (RMS) values (CRVs) of V_T^s and V_R^s computed from the dual-Doppler-analyzed VF field within $R \le 5$ km over the entire depth of the analysis domain (see the end of section 4), we can set the background error amplitude to $\sigma_1 = 15$ m s^{-1} for V_T^s and to $\sigma_R = 10$ m s^{-1} for V_R^s with the background term reinterpreted as a regularization term in the cost function for stand-alone applications (as explained at the end of the conclusion section in Part I). The background error amplitude for ψ^s can be then estimated by $\sigma_2 \approx \sigma_R H_2$ [see (3.2) of Part II]. Thus, in summary, we can set $\sigma_1 = 15$ m s^{-1}, $l = l_1 = 1/2$ and $H = H_1 = 2$ km for V_T^s and set $\sigma_2 = \sigma_R H_2$

with $\sigma_R = 10$ m s^{-1}, $l = l_2 = 1$, and $H = H_2 = 1$ km for ψ^s in the covariance functions formulated in (3.8) of Part I.

For the asymmetric part of (V_T, V_R) or (u', v'), denoted by $\mathbf{u}^a \equiv (u^a, v^a)$, the rotational-component velocity field should have narrower and deeper structures than the divergent-component velocity field and so do their corresponding background error fields. Based on this consideration, we can set $l = l_3 = 1$ and $H = H_3 = \sqrt{3}$ km for the vertically integrated velocity potential X associated with the divergent component of $\mathbf{u}^a$ but set $l = l_4 = 1/\sqrt{2}$ and $H = H_4 = 2$ km for the streamfunction Y associated with the rotational component of $\mathbf{u}^a$, where X and Y are the control variables defined in (4.4) of Part I. For the above settings of $l_3 = 1$ and $l_4 = 1/\sqrt{2}$, the corresponding radial decorrelation lengths at $R = R_c$ in the physical space are $L_3 = \sqrt{2}R_c \approx 2$km and $L = L_4 \approx R_c = 1.5$ km, respectively.

Consistent with the CRVs of u^a and v^a computed from the dual-Doppler-analyzed VF field (see the end of section 4), the background error standard deviation can be set to $\sigma_a = 10$ m s^{-1} for u^a and v^a. The background error variance of $\mathbf{u}^a$ is thus given by $2\sigma_a^2$. Assume that the background error variance of $\mathbf{u}^a$ is equally partitioned between its rotational and divergent parts, so the background error variance for each part is given by σ_a^2. The background error standard deviation for X (or Y) can be then estimated by $\sigma_3 = \sigma_a L_3 H_3/\sqrt{2}$ (or $\sigma_4 = \sigma_a L_4/\sqrt{2}$) according to (A.13)–(A.14) of Xu et al. (2010) and (3.2) of Part II. Thus, in summary, we can set $\sigma_3 = \sigma_a L_3 H_3/\sqrt{2}$ with $\sigma_a = 10$ m s^{-1}, $L_3 = 2$ km, $l = l_3 = 1$ and $H = H_3 = \sqrt{3}$ km for X and set $\sigma_4 = \sigma_a L_4/\sqrt{2}$ with $L_4 = \sqrt{2}$ km, $l = l_4 = 1/\sqrt{2}$ and $H = H_4 = 2$ km for Y in the covariance functions formulated in (4.8) of Part I.

4. Application to dual-Doppler radial-velocity observations

The VF-Var is applied to the KTLX and PAR radial-velocity observations within the analysis domain (see Fig. 4). The analyzed axisymmetric fields of V_T^s and (V_R^s, w^s) are plotted as functions of (R, z') by color contours and back arrows, respectively, in Fig. 5a. As shown, V_T^s increases rapidly from 0 to a maximum (which varies between 24 and 39 m s^{-1} as z' varies between 0 and 5 km) as R increases from 0 to about 0.6 km on each vertical level, and then decreases gradually as R further increases. The vector field of (V_R^s, w^s) shows a strong downdraft within the vortex core surrounded by an annular updraft over the broad area outside the radial range of $R = 1.5$ km. The central-downdraft velocity reaches a minimum of $w^s = -35.2$ m s^{-1} at $z' = 3$ km, while the surrounding-updraft velocity increases to $w^s = 26.1$ m s^{-1} at $(R, z') = (2.75, 5.0)$ km.

As defined in section 2b of Part I, the tangential, radial, and vertical components of the asymmetric-part VF, denoted by (V_T^a, V_R^a, w^a), should have zero azimuthal means. This condition, however, is not exactly satisfied by the second-step analyzed asymmetric VF, so the total symmetric VF should be diagnosed by $(V_T^{s+}, V_R^{s+}, w^{s+}) = (V_T^s, V_R^s, w^s) + (V_T^{as}, V_R^{as}, w^{as})$, where $(V_T^{as}, V_R^{as}, w^{as})$ is the nonzero azimuthal means of (V_T^a, V_R^a, w^a) as explained in section 4a of Part II. As shown in

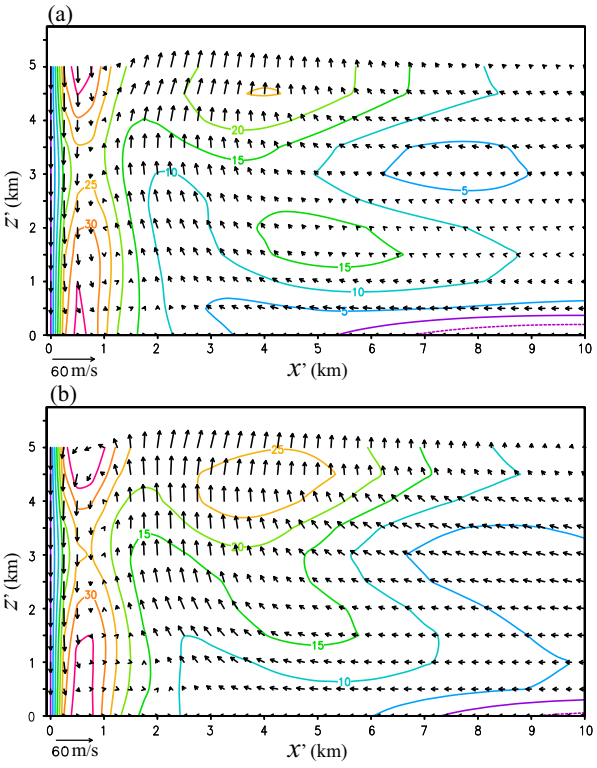

FIG. 5. (a) Dual-Doppler-analyzed V_T^s and (V_R^s, w^s) plotted by color contours (every 5 m s^{-1}) and black arrows in (R, z') with the vector scale shown in the lower-left corner. (b) As in (a), but for dual-Doppler diagnosed V_T^{s+} and (V_R^{s+}, w^{s+}).

Fig. 5b, the diagnosed V_T^{s+} is similar to V_T^s in Fig. 5a especially within the 5-km radial range, and it reaches a maximum (which also varies between 24 and 39 m s^{-1} as z' varies between 0 and 5 km) as R increases from 0 to about 0.6 km on each vertical level, while the negative V_T^s in the surface layer (below $z' = 0.4$ km) outside the 5-km radial range is largely offset by the positive V_T^{as}. The diagnosed vector field of (V_R^{s+}, w^{s+}) in Fig. 5b is also similar to (V_R^s, w^s) in Fig. 5a especially within the 5 km radial range. Thus, the analyzed axisymmetric fields largely capture the diagnosed total axisymmetric fields especially within the 5-km radial range, and they both reveal that the axisymmetric part of the tornadic mesocyclone is a well-defined slantwise two-cell vortex. This slantwise two-cell vortex is a variant of the previously depicted upright two-cell vortex model (Davies-Jones 1986; Davies-Jones et al. 2001; Wood and Brown 2011) and also a variant of the upright axisymmetric two-cell vortex diagnosed from mobile radar observations of the 3 May 1999 Mulhall, Oklahoma, tornado (Lee and Wurman 2005, see their Figs. 4 and 9).

The axisymmetric and asymmetric combined total VF field, $(\mathbf{u}', w') = (\mathbf{u}^s, w^s) + (\mathbf{u}^a, w^a)$, produced in (x', y', z') by the dual-Doppler analysis is shown on four different vertical levels (at $z' = 1$, 2, 3, and 4 km) in Fig. 6. At $z' = 1$ km, as shown in Fig. 6a, the $\mathbf{u}'$ field circulates tightly and cyclonically into a nearly axisymmetric vortex core within 1 km radial range from the vortex center. Along the edge of this vortex core,

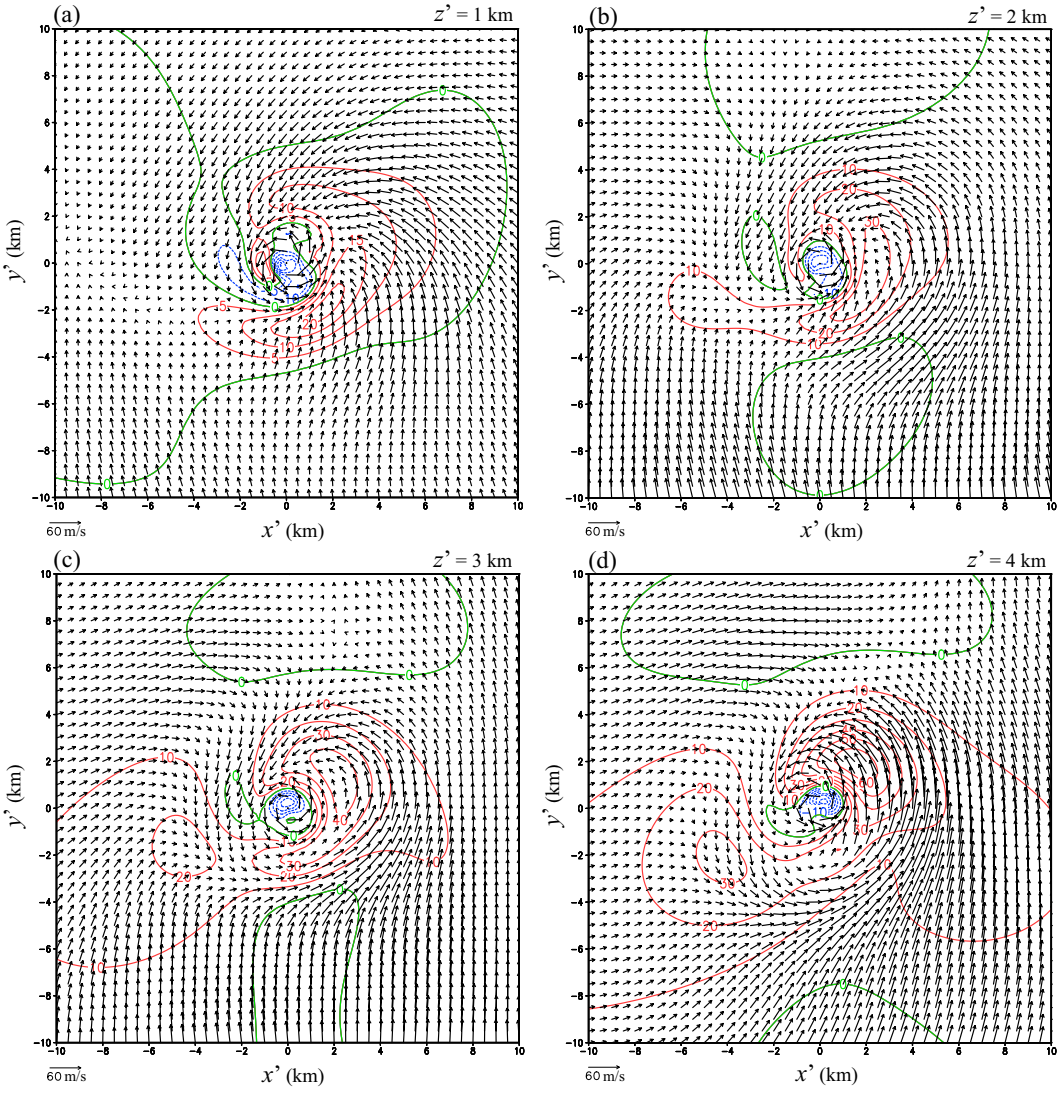

FIG. 6. Dual-Doppler-analyzed ($\mathbf{u}'$, w') in (x', y', z') with $\mathbf{u}'$ plotted by black arrows and w' plotted by red, green, and blue contours for positive, zero, and negative values, respectively, at z' = (a) 1, (b) 2, (c) 3, and (d) 4 km in the analysis domain. The contour intervals are every 5 m s^{-1} in (a) and every 10 m s^{-1} in (b) and (c). The vector scale is shown in the lower-left corner in each panel.

the horizontal wind is very strong and reaches a maximum speed of $|\mathbf{u}'| = 41.9$ m s^{-1} at $(x', y') = (0.75, -0.25)$ km. However, the w' field in the vortex core is nonaxisymmetric and is characterized by a strong downdraft in the central vortex and southeast quadrant [where w' reaches a minimum of -26.5 m s^{-1} at $(x', y') = (-0.25, 0)$ km] with a weak updraft on the west side of vortex core. At $z' = 1$ km, this central downdraft is connected, on its southern end, westward to a weak downdraft whose area is curved around the vortex core and then connected northward to a broad area of weak downward motion farther away from the vortex core. The w' field in Fig. 6a also shows a banana-shaped area of main updraft to the southeast immediately outside the vortex core, where w' reaches a maximum of 22.0 m s^{-1} at $(x', y') = (1.75, -1.75)$ km. In and around this main updraft, the $\mathbf{u}'$ field is strongly convergent. The banana-shaped main-updraft area has a long tail that is curved around the northside of vortex core and then connected southward to the weak-updraft area on the west side of vortex core. In this way, the main updraft nearly encircles the central downdraft in the vortex core at $z' = 1$ km. Thus, at least around and below $z' = 1$ km, the total VF has a loosely defined two-cell vortex structure, which is somewhat similar to the two-cell vortex structures produced in the tornado-resolving ensemble predictions of the 20 May 2013 Newcastle–Moore tornado (Snook et al. 2019, see their Figs. 6a and 7a). Loosely defined two-cell vortex structures were also produced in the numerical prediction of the 8 May 2003 Oklahoma City tornadic supercell (Xue et al. 2014, see their Figs. 15a,b).

Below $z' = 1$ km and within the 5 km radial range, the $\mathbf{u}'$ field remains mostly the same as that at $z' = 1$ km and the w'

field has roughly the same pattern as that at $z' = 1$ km but with its amplitude gradually reduced to zero as z' decreases to zero. At $z' = 0$, the VF has a maximum of $|\mathbf{u}'| = 45.1$ m s^{-1} at $(x', y') = (0.5, -0.25)$ km, and the total wind speed has a maximum of $|\mathbf{u}| = |\mathbf{u}' + \mathbf{u}_c| = 51.2$ m s^{-1} at $(x', y') = (0.5, -0.25)$ km. The maximum wind at $z' = 0$ is thus on the southeast edge of vortex core, and this maximum-wind location relative to the vortex center is roughly consistent with that (at 10 m above the ground) from the tornado-resolving ensemble predictions of the 20 May 2013 Newcastle–Moore tornado (Snook et al. 2019, see their Fig. 6d or Fig. 7d).

Above $z' = 1$ km, as shown in Figs. 6b–d, the vortex core extends along the slantwise z' coordinate (see Fig. 3) and becomes slightly large as z' increases to and above 3 km. The central downdraft inside the vortex core also extends along the z' coordinate and becomes increasingly intense and concentrated around the vortex center as z' increases from 1 to 2 km [where w' reaches a minimum of -37.7 m s^{-1} at $(x', y') = (-0.25, 0)$ km]. Also, as z' increases from 1 to 2 km, the curved weak downdraft shrinks into an isolated elliptic area surrounded by upward motion (since this downward-motion area is disconnected not only from the central-downdraft area on its southern end but also from the broad weak downward motion area on the northern edge of the domain). As z' increases to and above 3 km, this isolated weak downdraft gradually merges into the central downdraft on the southwest side of vortex core. On the other hand, the weak updraft on the west side of vortex core shrinks northward back into the main updraft as z' increases to and above 2 km, while the main updraft becomes increasingly strong as z' increases to 4 km [where w' reaches a minimum of -65.6 m s^{-1} at $(x', y') = (0.25, 0.25)$ km]. As the main updraft extends upward, it spirals cyclonically around the vortex core. Along this spiral main updraft, the maximum w' in the updraft core increases successively from 22.0 m s^{-1} at $(x', y', z') = (1.75, -1.75, 1.0)$ km to 38.0 m s^{-1} at $(x', y', z') = (2.0, -1.0, 2.0)$ km, 47.3 m s^{-1} at $(x', y', z') = (2.25, 1.25, 3.0)$ km, and 67.1 m s^{-1} at $(x', y', z') = (1.5, 2.0, 4.0)$ km. Thus, the dual-Doppler-analyzed VF is a loosely defined slantwise two-cell vortex over the entire depth of the analysis domain.

Within $R \leq 5$ km over the entire depth of the analysis domain, the volume-averaged RMS values of the analyzed V_T^s and V_R^s are 16.0 and 5.9 m s^{-1}, respectively, while the volume-averaged RMS values of the analyzed u^a and v^a are 9.4 and 12.6 m s^{-1}, respectively. These RMS values support the specified background error amplitudes (i.e., $\sigma_1 = 15$ m s^{-1} for V_T^s, $\sigma_R = 10$ m s^{-1} for V_R^s, and $\sigma_a = 10$ m s^{-1} for u^a and v^a) in section 3, because the background error field is the true VF field (i.e., the true total wind field minus $\mathbf{u}_c$) and the dual-Doppler-analyzed VF is accurate enough to represent the true VF (see section 6).

5. Application to single-Doppler radial-velocity observations

The VF-Var is now applied to the dealiased single-Doppler velocity observations from KTLX radar only within the analysis domain. The analyzed axisymmetric fields of V_T^s and (V_R^s, w^s) are shown in Fig. 7a. As shown, the V_T^s field in Fig. 7a

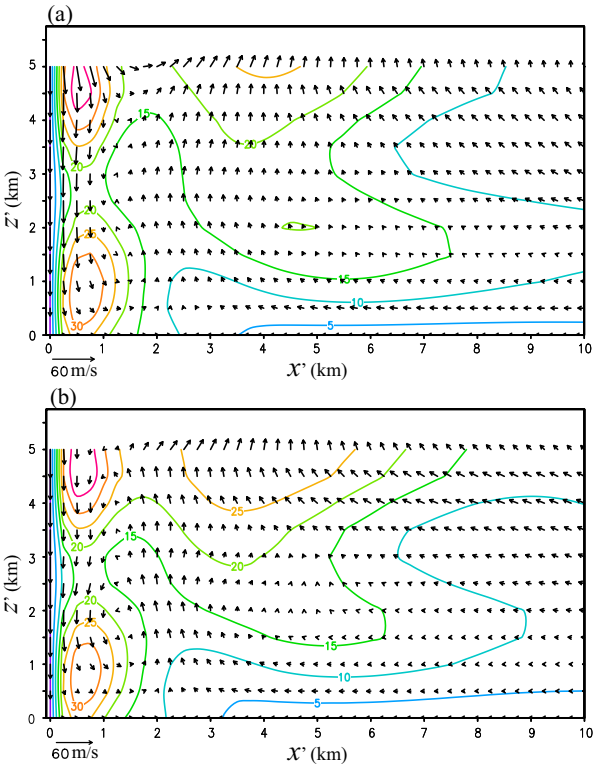

FIG. 7. As in Fig. 5, but for single-Doppler-analyzed V_T^s and (a) (V_R^s, w^s) and (b) (V_R^{s+}, w^{s+}).

is quite similar to the dual-Doppler-analyzed V_T^s in Fig. 5a especially within the radial range of $R \leq 5$ km. In particular, V_T^s in Fig. 7a also increases rapidly from 0 to a maximum (which varies between 19 and 38 m s^{-1} as z' varies between 0 and 5 km) as R increases from 0 to about 0.6 km on each vertical level, and then decreases gradually as R further increases to 2 km or beyond, although the maximum V_T^s is slightly lower than that in Fig. 5a for $z' \leq 3$ km and especially for $z' < 0.5$ km. The vector field of (V_R^s, w^s) in Fig. 7a is also quite similar to the dual-Doppler-analyzed (V_R^s, w^s) in Fig. 5a especially within the radial range of $R \leq 5$ km. In Fig. 7a, the central-downdraft velocity reaches a minimum of $w^s = -43.1$ m s^{-1} at $(R, z') = (0, 3)$ km, while the surrounding-updraft velocity increases to $w^s = 18$ m s^{-1} at $(R, z') = (3.5, 5)$ km, so the single-Doppler-analyzed central downdraft (or surrounding annular updraft) is stronger (or weaker) than the dual-Doppler-analyzed one in Fig. 5a.

The diagnosed V_T^{a+} and (V_R^{a+}, w^{a+}) from the single-Doppler analysis are shown in Fig. 7b, and they are largely the same as those in Fig. 7a especially within the 5 km radial range. As explained earlier, the single-Doppler-analyzed axisymmetric field in Fig. 7a is quite close to the dual-Doppler-analyzed in Fig. 5a, while the latter can largely capture the dual-Doppler diagnosed total axisymmetric field especially within the 5 km radial range, and so does the single-Doppler-analyzed axisymmetric field in Fig. 7a. Again, all these axisymmetric fields exhibit well-defined slantwise two-cell vortex structures.

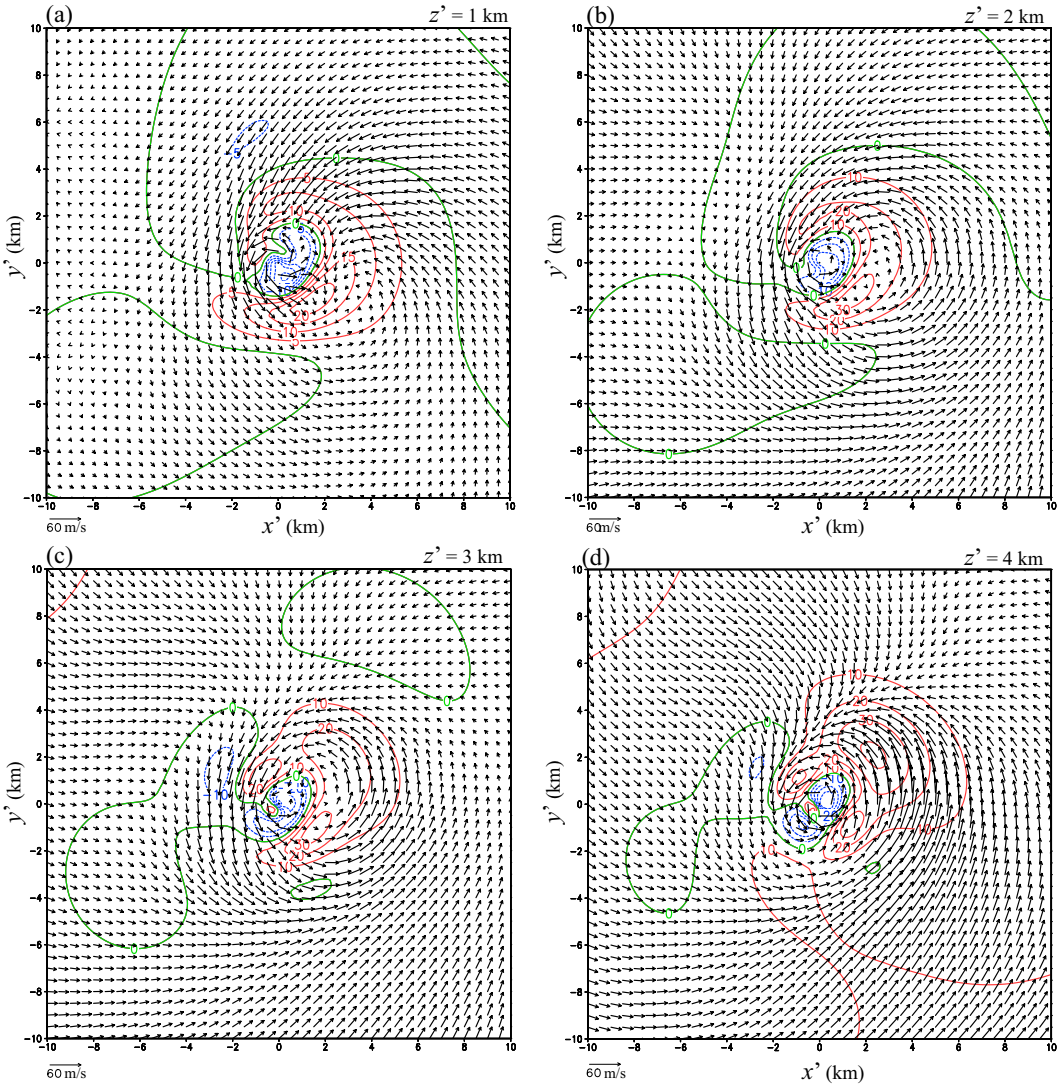

FIG. 8. As in Fig. 6, but for single-Doppler-analyzed ($\mathbf{u}'$, w').

The total VF field, ($\mathbf{u}'$, w'), produced by the single-Doppler analysis is shown on four different vertical levels (at z' = 1, 2, 3, and 4 km) in Fig. 8. At z' = 1 km, the $\mathbf{u}'$ field in Fig. 8a also shows a strong cyclonic vortex core around the center of the analysis domain and this vortex core is similar to the dual-Doppler analyzed in Fig. 6a. Along the edge of vortex core, the horizontal wind is also very strong [with a maximum $|\mathbf{u}'|$ of 45.2 m s^{-1} at (x', y') = (−0.75, −0.5) km] but the w' field inside the vortex core is more nonaxisymmetric than that in Fig. 6a. In particular, the central downdraft in the vortex core [where w' reaches a minimum of −26.2 m s^{-1} at (x', y') = (0.25, −0.5) km] is as strong as that in Fig. 6a but there is no updraft on the west side of the vortex core (so the curved tail of main-updraft area ends on the north side of vortex core). Also unlike that in Fig. 6a, the central-downdraft area in Fig. 8a is disconnected from the broad area of weak downward motion to the north farther away from the vortex core. The w' field in Fig. 8a also shows a banana-shaped main updraft to the southeast immediately outside the vortex core where w' reaches a maximum of 23.1 m s^{-1} at (x', y') = (1.5, −1.75) km, and this main updraft is very similar to that in Fig. 6a. In and around this main updraft, the $\mathbf{u}'$ field is also strongly convergent, similarly to that in Fig. 6a. The banana-shaped area of main updraft also has a long tail that encircles the central-downdraft area in the vortex core.

Again, below z' = 1 km and within the 5-km radial range, the $\mathbf{u}'$ field remains mostly the same as that at z' = 1 km and the w' field remains the same pattern but with its amplitude gradually reduced to zero as z' decreases to 0. At z' = 0, the single-Doppler-analyzed VF has a maximum of $|\mathbf{u}'|$ = 34.5 m s^{-1} at (x', y') = (−0.5, −0.75) km, and the total wind speed has a maximum of $|\mathbf{u}|$ = 40.7 m s^{-1} at (x', y') = (0, −0.75) km, which is smaller than the maximum of $|\mathbf{u}|$ from the dual-Doppler analysis in section 4.

Above z' = 1 km, as shown in Figs. 8b–d, the vortex core extends along the z' coordinate and becomes slightly large as

z' increases to and above 3 km, similarly to that in Figs. 6b–d. The central downdraft inside the vortex core also extends along the z' coordinate and becomes increasingly intense around the vortex center as z' increases from 1 to 2 km [where w' has a minimum of -37.4 m s^{-1} at $(x', y') = (0.5, -0.25)$ km]. This is similar to that shown in Fig. 6b, but the central-downdraft area at $z' = 2$ km in Fig. 8b is curved and connected westward to the weak-downdraft area outside the vortex core. As z' increases further to and above 3 km, the central downdraft splits into two branches with a small updraft in between, but this fine-scale structure is spurious (for reasons explained later in section 6) and is not seen from the dual-Doppler-analyzed fields in Figs. 6c and 6d. Besides, the main updraft also splits into two branches at and around $z' = 3$ km (see Fig. 8c) and further splits into three branches as z' increases to and above 4 km (see Fig. 8d). Clearly, although the single-Doppler-analyzed main updraft also becomes increasingly strong and spirals cyclonically around the vortex core as z' increases from 1 to 5 km, it is not as strong and spirals not as smoothly as the dual-Doppler-analyzed main updraft. In particular, the maximum w' in this spiral main updraft increases successively from 23.1 m s^{-1} at $(x', y', z') = (1.5, -1.75, 1)$ km to 35.6 m s^{-1} at $(x', y', z') = (1.5, -1.25, 2)$ km, 35.4 m s^{-1} at $(x', y', z') = (1.5, -1.25, 3)$ km, and 41.9 m s^{-1} at $(x', y', z') = (2.25, 2.25, 4)$ km. Thus, the single-Doppler-analyzed VF still has a loosely defined slantwise two-cell vortex structure over the entire depth of the analysis domain, but this two-cell vortex structure is more loosely defined than its dual-Doppler-analyzed counterpart.

The VF-Var is also applied to single-Doppler observations from PAR only, and the analyzed VF (see Fig. A1 in appendix A) contains more spurious structures than the single-Doppler-analyzed VF in Fig. 8, especially at and above 3 km-height due to the shortage (or lack) of observations from PAR above 3 (or 4)-km height (see Fig. 4b).

6. Analysis error assessments

As explained in section 2, the vortex center axis, $\mathbf{x}_c(z, t)$, is estimated by fitting smooth-function forms [see (1)–(5) of Xu et al. 2017] to the discrete data of $\mathbf{x}_{ci}$ in the two-dimensional space of (z, t), while $\mathbf{x}_{ci}$ is the vortex center location estimated individually at the i^{th} discrete point, (z_i, t_i), as a by-product of the mesocyclone-targeted dealiasing (Xu and Nai 2017). As a smooth vector function of (z, t), the true vortex center axis is likely between the estimated $\mathbf{x}_c(z, t)$ and $\mathbf{x}_{ci}$, so the error/uncertainty of estimated $\mathbf{x}_c(z, t)$ can be assessed by $\|\Delta\mathbf{x}_{ci}\|/2$ with the error upper bound estimated by $\|\Delta\mathbf{x}_{ci}\|$, where $\Delta\mathbf{x}_{ci} \equiv \mathbf{x}_{ci}-\mathbf{x}_c(z_i, t_i)$ is the residual at the i^{th} discrete point, $\|\Delta\mathbf{x}_{ci}\| \equiv \left[\sum_i |\Delta\mathbf{x}_{ci}|^2\right]^{1/2}$ is the RMS value of $|\Delta\mathbf{x}_{ci}|$, and $\sum_i$ denotes the summation over i. From the values of $(\Delta x_{ci}, \Delta y_{ci}) = \Delta\mathbf{x}_{ci}$ listed in the caption of Fig. 2, the computed value of $\|\Delta\mathbf{x}_{ci}\|$ is 0.3 km or $R_1/2$, where R_1 is the vortex core radius (about 0.6 km as assessed from Fig. 5b). Thus, the error/uncertainty of estimated $\mathbf{x}_c(z, t)$ is about $R_1/4$ and bounded by $R_1/2$.

As shown in Part II and Part III, the VF-Var can be very accurate for a dual-Doppler analysis if $\mathbf{x}_c$ is accurately estimated, but the analysis accuracy will reduce substantially when $\mathbf{x}_c$ is not accurately estimated. In particular, the cylindrical-volume-averaged RMS error (CRE) will increase from 0.4–0.5 to about 1.8 m s^{-1} for each component of dual-Doppler-analyzed (u', v') and from 1.5–1.9 to around 3.5 m s^{-1} for dual-Doppler-analyzed w' if the vector distance of the estimated $\mathbf{x}_c$ from the true $\mathbf{x}_c$ increases from zero to $\mathbf{e}R_1/4$ (see Tables 4 and 5 of Part III), where

$$\mathbf{e} \equiv \left[-\cos(\pi z/D - \pi/4),\ -\sin(\pi z/D)\right] \tag{6.1}$$

is a vector function of z as defined in (2.2) of Part III, $D = 5$ km is the analysis domain height, and the cylindrical-volume average is taken over the volume within $R \le 5$ km through the entire 5-km depth of analysis domain. In this case, the analysis errors are caused mainly by the error/uncertainty of $\mathbf{x}_c$ measured by $\mathbf{e}R_1/4$.

For the dual-Doppler analysis presented in section 4, the analysis error is very likely caused also mainly by the error/uncertainty of $\mathbf{x}_c$, because the error/uncertainty of $\mathbf{x}_c$ is between $R_1/4$ and $R_1/2$ as estimated earlier. In this case, the lower (or upper) bound of CRE can be assessed for each component of dual-Doppler-analyzed (u', v', w') by the cylindrical-volume-averaged RMS value (CRV) for each component of $(\Delta u', \Delta v', \Delta w')$, where $(\Delta u', \Delta v', \Delta w')$ are the perturbations caused in the dual-Doppler-analyzed (u', v', w') when the estimated $\mathbf{x}_c$ (shown in Figs. 2 and 3) is perturbed by a vector distance of $\mathbf{e}R_1/4$ (or $\mathbf{e}R_1/2$). The assessed lower (or upper) bound of CRE and associated lower (or upper) bound of RCRE are listed for each component of dual-Doppler-analyzed (u', v', w') in row 1 (or 2) of Table 1, where RCRE stands for relative CRE defined by the ratio of CRE to the CRV of the same velocity component from dual-Doppler analysis.

Note that the CRVs of (u', v', w') are (15.2, 15.3, 9.4) m s^{-1} for the benchmark VF in Part III but increased to (15.6, 22.0, 20.0) m s^{-1} for the dual-Doppler-analyzed VF in this paper, so only the RCREs in Table 1 can be directly compared with those in Table 5 of Part III. Specifically, the lower (or upper) bound of RCRE assessed for each component of dual-Doppler-analyzed (u', v', w') in row 1 (or 2) of Table 1 can be compared with the increment of RCRE for the same velocity component from row 1 to row 2 (or 3) in Table 5 of Part III, because these RCRE increments are caused purely/solely by perturbing $\mathbf{x}_c$ away from the true $\mathbf{x}_c$ by a vector distance of $\mathbf{e}R_1/4$ (or $\mathbf{e}R_1/2$). The RCRE increments, calculated by subtracting the RCREs in row 1 from those in row 2 (or 3) of Table 5 in Part III, are (8%, 7%, 19%) [or (18%, 17%, 45%)] for (u', v', w'). The above RCRE increments of (8%, 19%) [or (18%, 45%)] for (u', w') are very close to the lower (or upper) bounds of RCREs assessed for (u', w') in Table 1, so these RCRE increments may remain useful for assessing the lower and upper bounds of RCRE for the dual-Doppler-analyzed (u', w') in this paper, even though the benchmark VF in Part III is structurally different from the real VF analyzed in this paper. However, the lower (or upper) bound of RCRE assessed by 13% (or 30%) for v' in row 1 (or 2) of Table 1 is nearly twice larger than the above RCRE increment of

TABLE 1. Lower (or upper) bounds of CRE and RCRE assessed for each component of dual-Doppler-analyzed (u', v', w') listed in row 1 (or 2), and lower bounds of CRE and RCRE assessed for each component of single-Doppler-analyzed (u', v', w') listed in row 3. Here, CRE stands for cylindrical-volume-averaged RMS error, RCRE stands for relative CRE defined by the ratio of CRE to the cylindrical-volume-averaged RMS value of the same velocity component field from dual-Doppler analysis, and the cylindrical-volume average is taken over the volume within $R \leq 5$ km through the entire 5-km depth of the analysis domain.

		CRE (m s^{-1})			RCRE (%)		
Analysis	Bound	u'	v'	w'	u'	v'	w'
Dual Doppler	Lower bound	1.2	2.9	5.0	9	13	25
	Upper bound	2.4	6.4	8.9	17	30	45
Single Doppler	Lower bound	3.5	13.6	10.3	22	62	52

7% (or 17%) for v'. This discrepancy can be explained by the partially reduced observability of v', because the KTLX site is to the east and the PAR site is to the southeast of the analysis domain (see Fig. 1) and therefore the two radar sites are separated with respect to the analysis domain by about 45° rather than 90° as in the idealized case (see Fig. 2 of Part II). As v' is still partially observable, the lower (or upper) bound of RCRE assessed for v' in row 1 (or 2) of Table 1 is much smaller than the RCRE increment of 24% (or 57%) for single-Doppler-analyzed v', as indicated by the RCRE for v' in row 5 (or 6) minus that in row 4 in Table 5 of Part III.

For the single-Doppler analysis in section 5, the analysis error is likely caused by both the lack of observability of v' and the error/uncertainty of $\mathbf{x}_c$, as suggested by the CREs listed for single-Doppler analyses in rows 4–6 of Table 5 in Part III. Thus, the analysis error cannot be reliably estimated in the same way as shown above for the dual-Doppler analysis, but can be assessed by using the dual-Doppler-analyzed VF to represent the unknown true VF (for reason explained later). In particular, the lower bound of CRE for each component of single-Doppler-analyzed (u', v', w') can be assessed by the CRV of the difference between the single-Doppler-analyzed VF and dual-Doppler-analyzed VF for the same velocity component. The assessed lower bound of CRE and associated lower bound of RCRE are listed for each component of single-Doppler-analyzed (u', v', w') in row 3 of Table 1. These assessed lower bounds are much higher than those for the dual-Doppler-analyzed VF in row 1 of Table 1, and this justifies the use of the dual-Doppler-analyzed VF to represent the true VF in the above assessment. The RCREs in row3 of Table 1 are within ±25% of those listed in row 5 of Table 5 of Part III, that is, (19%, 40%, 77%) for single-Doppler-analyzed (u', v', w') with $\mathbf{x}_c$ deviated away from the true $\mathbf{x}_c$ by $\mathbf{e}R_1/4$. Thus, the RCREs in row 5 of Table 5 of Part III may also remain useful for assessing the RCREs for the single-Doppler-analyzed (u', v', w') in this paper, although the benchmark VF in Part III is structurally different from the real VF analyzed in this paper.

7. Applications to other dual-Doppler radial-velocity observations

The VF-Var is also applied to Doppler velocity observations collected in additional 7 volume scans from the KTLX radar and 14 rapid sector scans from the PAR over 14 partially overlapped analysis time windows between 2003 and 2034 UTC for the 20 May 2013 Newcastle–Moore tornadic mesocyclone. The vortex center axis is still estimated as a continuous function of height and time but over the entire 31-min time period (see Fig. B1 in appendix B). The dual-Doppler-analyzed VFs are shown by the three examples in appendix B. These dual-Doppler-analyzed VFs reveal that the main structure of analyzed VF field changes gradually but the fine structures of vortex winds especially vertical motions in and near the vortex core change rapidly as the analysis time window shifts. This implies that transient fine structure variations were too rapid to resolve by these dual-Doppler-analyzed VF fields (because each analyzed VF field is a time-averaged field over the 4- or 5-min analysis time window and the 14 partially overlapped analysis time windows have a limited temporal resolution, which is about 2 min).

8. Conclusions

In this paper, the VF-Var formulated in Part I is applied to Doppler velocity observations of the 20 May 2013 Newcastle–Moore tornadic mesocyclone in Oklahoma. These velocity observations were collected and dealiased in one volume scan from the KTLX radar and one rapid sector scan from the PAR over the time period from 2003:50 to 2007:50 UTC that defines the 4-min analysis time window. The vortex center axis of the mesocyclone is estimated as a continuous function of height and time (see Figs. 2 and 3) and is used as the vertical coordinate in the vortex-following coordinate system [see (2.1)], in which the time-averaged VF field over the 4 min analysis time window is expressed in terms of covariance basis vectors (see Fig. 1b and Table 1 of Part I). Since this VF field is analyzed in the vortex-following coordinate system with the background velocity field given by the vortex center moving velocity, the background error field is simply the true VF field and can be largely represented by the dual-Doppler-analyzed VF in this paper. Based on this consideration, the background error covariance parameter values used in the VF-Var are estimated and specified based on the structure of true background error field represented approximately by the dual-Doppler-analyzed VF field. The dual-Doppler analysis is performed (in section 4) with the radial-velocity observations from both KTLX radar and PAR. The analysis domain is a cubic box of $20 \times 20 \times 5$ km^3 in the vortex-following coordinate system and thus is a time-varying slantwise cubic box in the physical space.

The dual-Doppler-analyzed VF field reveals the following features:

(i) The axisymmetric part of VF is a well-defined slantwise two-cell vortex (see Figs. 5a,b). In this two-cell vortex, the maximum tangential velocity is nearly 40 m s^{-1} at the edge of vortex core (about 0.6 km from the vortex

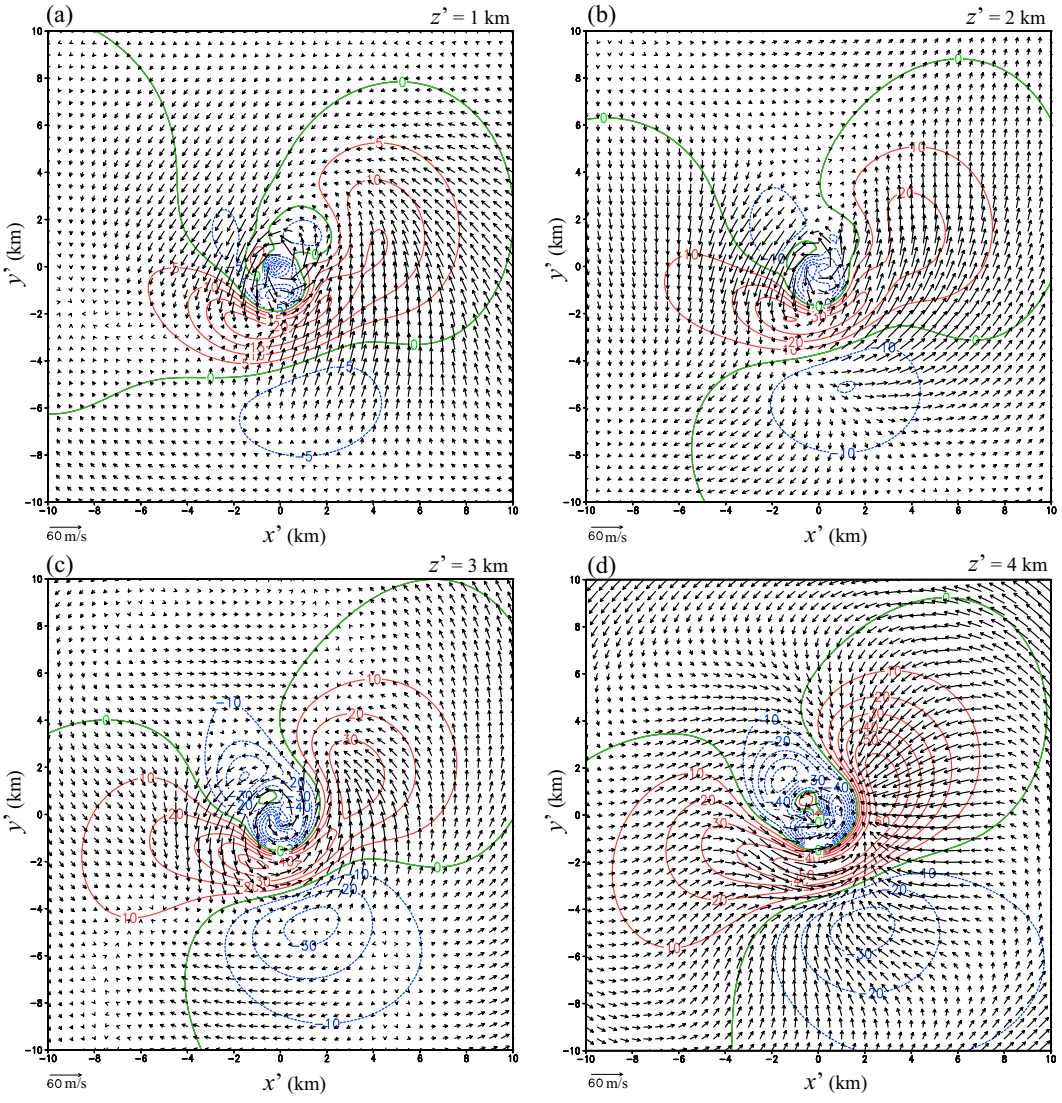

FIG. A1. As in Fig. 6, but for single-Doppler-analyzed ($\mathbf{u}'$, w') obtained by applying the VF-Var to the dealiased radial-velocity observations from PAR only (scanned from 2004:40 to 2005:24 UTC, as described in section 2 and shown in Fig. 4b).

center), the central-downdraft velocity reaches a negative maximum of -35 m s^{-1} at 3-km height, and the vertical velocity in the surrounding annular updraft increases with height to a maximum of 26 m s^{-1} nearly 3 km away from the vortex center at 5-km height.

(ii) The axisymmetric and asymmetric-part combined total VF field is a loosely defined slantwise two-cell vortex with the following detailed features (see Figs. 6a–d): The horizontal flow circulates tightly and cyclonically around the vortex center forming a nearly axisymmetric vortex core. On the southeast edge of the vortex core, the system-relative (or ground-relative) surface wind speed reaches a maximum of 45 (or 50) m s^{-1}. The vertical circulation consists primarily of a strong nonaxisymmetric slantwise downdraft (with a maximum downward velocity of -66 m s^{-1} at 4-km height) in the vortex core and a main updraft in a banana-shaped core area southeast of the vortex core above the ground. A long curved tail area of upward motion is stretched from this updraft core area northward and then spiraled into the west side of vortex core. As the main updraft extends slantwise upward, it spirals cyclonically around the vortex core and the maximum vertical velocity in the updraft core increases from 22 m s^{-1} at 1 km to 67 m s^{-1} at 4 km above the ground. This main updraft nearly encircles the central downdraft in the vortex core over the entire 5 km depth of analysis domain.

By applying the VF-Var to observations from KTLX radar only, the single-Doppler-analyzed VF field exhibits roughly the same features as the dual-Doppler analysis especially for

the axisymmetric part, although the single-Doppler-analyzed central downdraft (or surrounding annular updraft) is stronger (or weaker) than the dual-Doppler-analyzed one. The single-Doppler-analyzed total VF also has a loosely defined slantwise two-cell vortex structure over the entire depth of analysis domain, but this two-cell vortex is more loosely defined than the dual-Doppler-analyzed one. In particular, the single-Doppler-analyzed central downdraft splits into two branches with a small updraft in between at and above 3-km height, while the single-Doppler-analyzed main updraft is not only weaker and spirals less smoothly than the dual-Doppler-analyzed counterpart but also splits into two (or three) branches at 3 (or 4)-km height.

The error/uncertainty in the estimated vortex center axis is assessed from fitting residuals when the vortex center axis is estimated by fitting smooth functions to the discrete data of individually estimated vortex center locations. The assessed error is about a quarter of the vortex core radius and no more than a half of the radius of vortex core. Using this assessed error with the findings from Part III, analysis errors are assessed for the dual-Doppler and single-Doppler-analyzed VFs in this paper. The results (see Table 1) indicate that the dual-Doppler-analyzed VF has adequate accuracies in all the three component velocities but the single-Doppler-analyzed VF can barely be accurate except for the primarily observed component velocity. In either case, as indicated by the findings from Part III, analysis errors in the vortex core should be larger than those outside the vortex core. Regardless of large vertical velocity errors in the vortex core, the dual-Doppler-analyzed VF should be able to represent the true VF approximately not only outside but also inside the vortex core. The single-Doppler-analyzed VF captures the gross structure of true VF (represented by the dual-Doppler-analyzed VF) but contains spurious structures especially for the vertical velocity field in and around the vortex core.

The VF-Var is also applied to Doppler velocity observations collected in additional 7 volume scans from the KTLX radar and 14 rapid sector scans from the PAR between 2003 and 2034 UTC for the 20 May 2013 tornadic mesocyclone. The dual-Doppler-analyzed VFs (shown by the examples in appendix B and highlighted in section 7) reveal that the main structure of analyzed VF field changes gradually as the analysis time window shifts, but the fine structures of vortex winds especially vertical motions in and near the vortex core change abruptly so their transient variations are not resolved (due to the limited temporal resolution, about 2 min, of the 14 partially overlapped analysis time windows associated with the 14 rapid sector scans from the PAR). Nevertheless, these dual-Doppler-analyzed VFs should be useful for initializing/verifying high-resolution tornado simulations of this particular tornadic mesocyclone, although continued research efforts are required to resolve transient fine structure variations in and around vortex cores when the VF-Var is applied in the near future to very rapid scans (every 10 s) of tornadic mesocyclones from mobile radars (Kurdzo et al. 2017).

Acknowledgments. The authors are thankful to Jidong Gao and two anonymous reviewers for their constructive comments and suggestions, and to Pamela Heinselman, Pengfei Zhang, and David Priegnitz for their help with the PAR data. The research work was supported by the NSSL Warn-on-Forecast project and the Office of Naval Research under Award N000142012449 to the University of Oklahoma (OU). Funding was also provided by NOAA/Office of Oceanic and Atmospheric Research under NOAA–OU Cooperative Agreement NA16OAR4320072, U.S. Department of Commerce. The numerical experiments were performed at the OU Supercomputing Center for Education and Research.

Data availability statement. Data used/produced in this study are archived at https://drive.google.com/file/d/1qW2DYuySsd4lA2UA8nyDnonWq0Fw3eK/view?usp=sharing, which are accessible for users within NOAA. For users outside NOAA, please contact the corresponding author Qin Xu for permission to access the data.

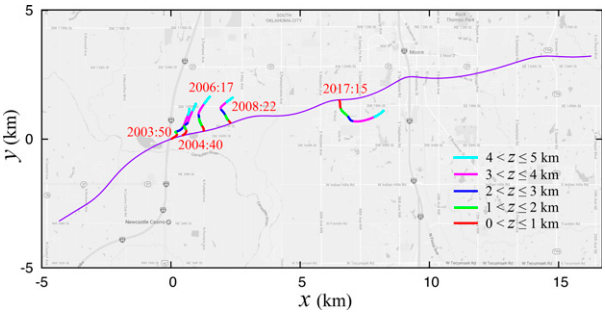

FIG. B1. Vertical variations of estimated vortex center axis $\mathbf{x}_c(z, t)$ viewed aloft strictly downward at five different times (labeled red in UTC) plotted by color-segmented curves atop the trajectory of $\mathbf{x}_c(0, t)$ (solid dark purple) superimposed on a highway and Moore city street map (printed in gray from Google Maps). The first (2003:50 UTC) is the beginning time of the analysis time window for the dual-Doppler analyses in section 5 and section a of appendix B (i.e., $t = 0$ in Fig. 3). The second (2004:40 UTC) is the beginning time of PAR sector-volume scan used by the dual-Doppler analyses in section 5. The third (2006:17 UTC) is the beginning time of PAR sector-volume scan used by the dual-Doppler analyses in section a of appendix B. The fourth (2008:22 UTC) is the beginning time of the analysis time window for the dual-Doppler analyses in section b of appendix B. The fifth (2017:15 UTC) is the beginning time of the analysis time window for the dual-Doppler analyses in section c of appendix B. As in Fig. 3, the origin of (x, y) is at $\mathbf{x}_c(0, 0)$—the estimated vortex center location at $(z, t) = (0, 0)$, and the five colored segments (in red, green, blue, purple, and cyan) of vortex center axis at each time indicate the estimated vortex center axis in five different vertical layers of 1 km depth from $z = 0$ to 5 km.

APPENDIX A

Single-Doppler Analysis with PAR Observations

The VF-Var is also applied to the dealiased single-Doppler velocity observations from PAR only (scanned from 2004:40 to 2005:24 UTC, as described in section 2 and shown in Fig. 4b). The analyzed $(\mathbf{u}', w')$ fields are shown at $z' = 1$, 2, 3, and

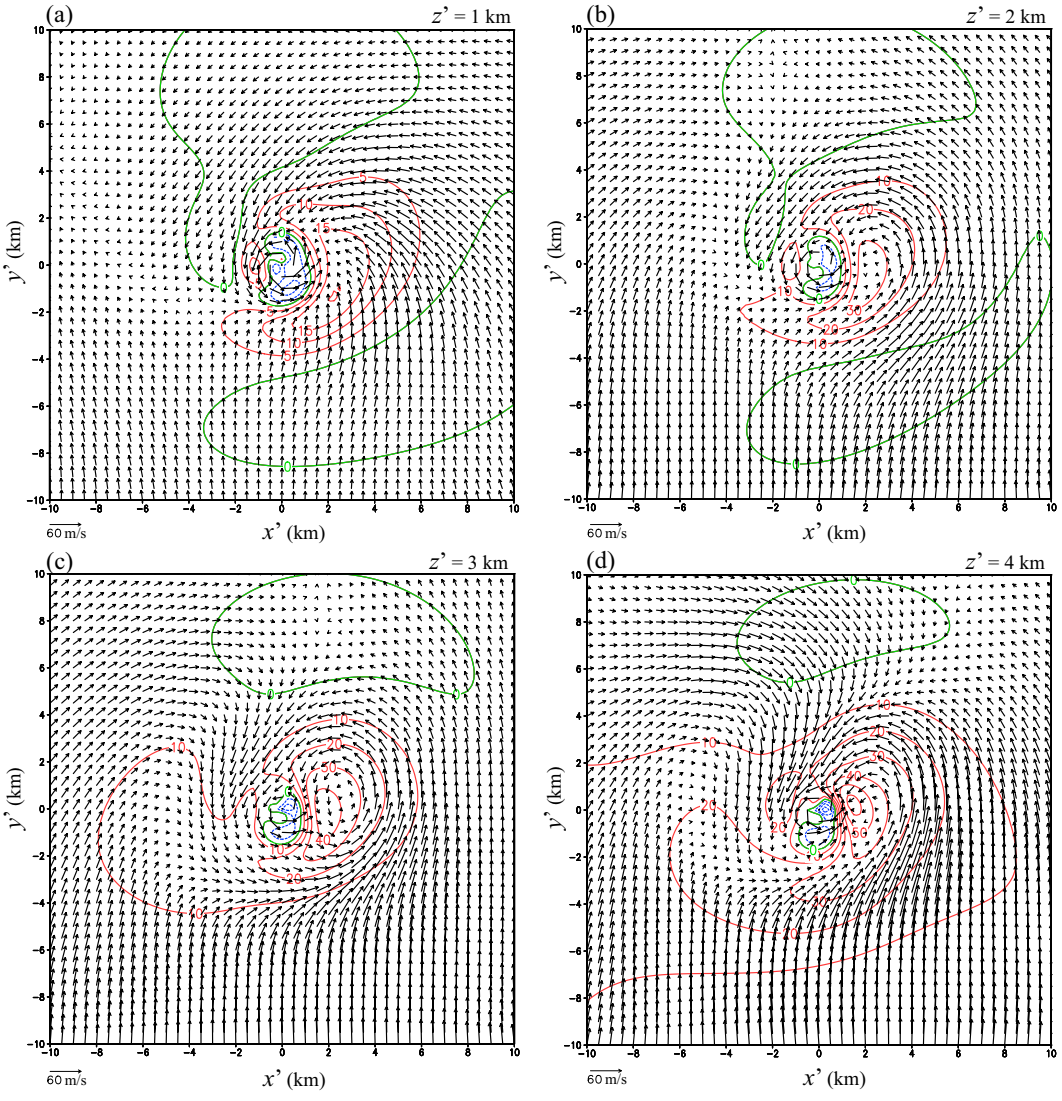

FIG. B2. As in Fig. 6, but for dual-Doppler-analyzed ($\mathbf{u}'$, w') obtained with the dealiased radial-velocity observations from PAR shifted to the next sector volume (scanned from 2006:17 to 2007:06 UTC).

4 km in the four panels of Fig. A1. By using the dual-Doppler-analyzed VF dual-Doppler-analyzed VF in Fig. 6 to represent the true VF approximately, visual comparisons can be made to identify more spurious structures in this single-Doppler-analyzed VF than that in Fig. 8, especially for the fields at $z' = 3$ and 4 km. The lower bounds of CREs can be assessed for this single-Doppler-analyzed VF in the same way as described in section 6 for the single-Doppler-analyzed VF in Fig. 8. The assessed lower bounds are (13.8, 23.2, 20.6) m s^{-1} for (u'', v'', w'), where $u'' \equiv u'\cos(\pi/4) - v'\sin(\pi/4) = (u' - v')/\sqrt{2}$ and $v'' \equiv u'\sin(\pi/4) + v'\cos(\pi/4) = (u' + v')/\sqrt{2}$ are the two components of $\mathbf{u}'$ in the (x'', y'') coordinate system that is rotated clockwise by 45° from the (x', y') coordinate system. Note that u'' (or v'') is the component of $\mathbf{u}'$ that is largely observable (or unobservable) by PAR. This explains why the assessed error is much larger for v'' than for u''. Besides, w' is also largely unobservable by PAR, and this explains why its error is also much larger than that for u''.

The lower bounds of circular-area-averaged RMS errors can be also assessed for the single-Doppler-analyzed VF in Fig. A1, where the circular-area average is taken over the area within $R \leq 5$ km on each given vertical level in the analysis domain. The assessed lower bounds are (2.9, 12.4, 5.7), (5.6, 17.2, 12.8), (7.3, 13.1, 21.0), and (18.5, 28.9, 28.5) m s^{-1} for (u'', v'', w') at $z' = 1$, 2, 3, and 4 km, respectively. The assessed error bounds at $z' = 1$ and 2 (or 3 and 4) km are close to (or much larger than) those listed in row 3 of Table 1 for the single-Doppler-analyzed VF in Fig. 8. The increased errors at $z' = 3$ and 4 km are consistent with the above visual comparisons and can be explained by the shortage (or lack) of observations from PAR at and above $z' = 3$ (or 4) km (see Fig. 4b).

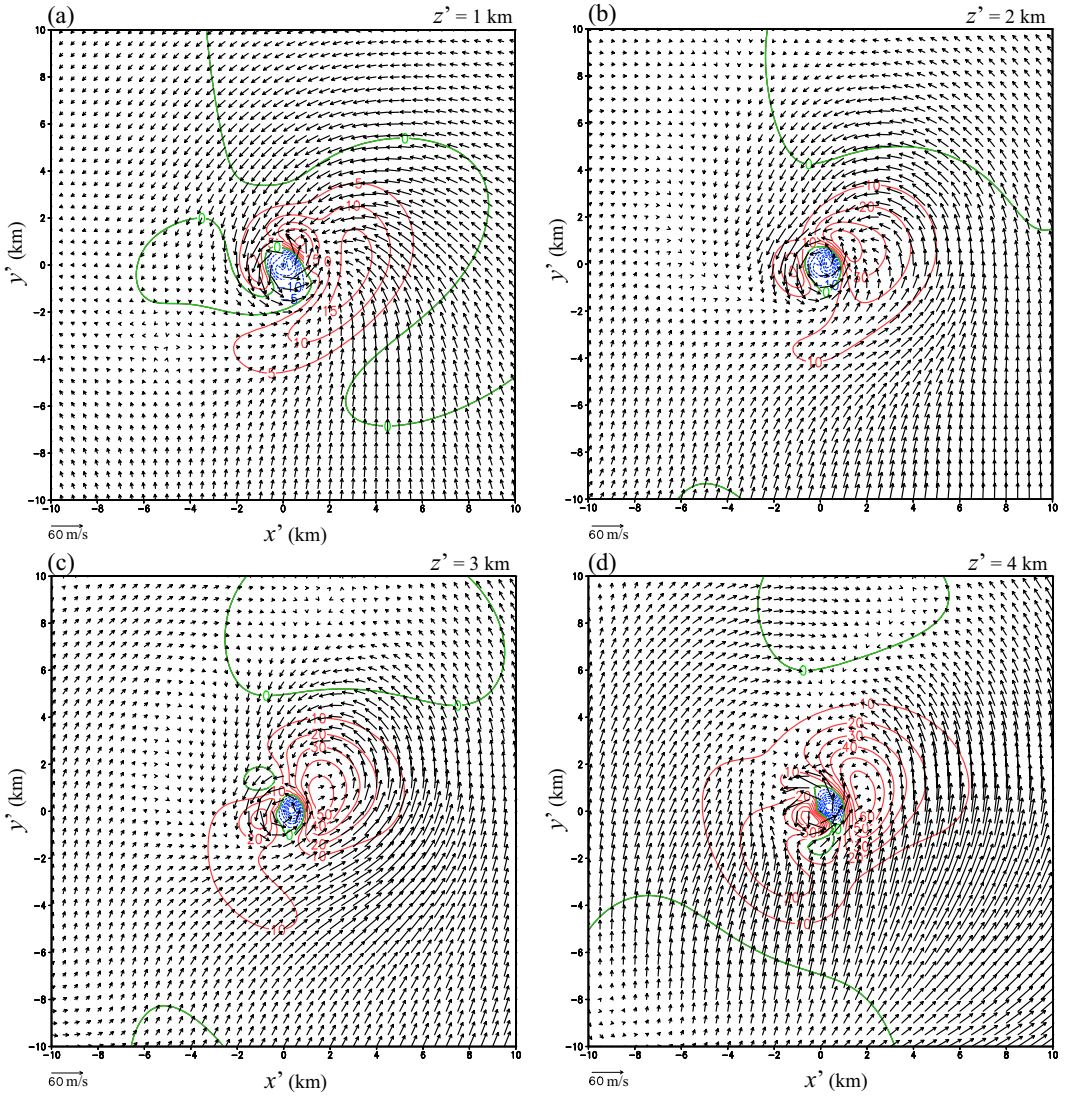

FIG. B3. As in Fig. B2, but for dual-Doppler-analyzed ($\mathbf{u}'$, w') obtained with the dealiased radial-velocity observations from KTLX radar shifted to the next volume (scanned from 2008:42 to 2012:22 UTC) and the dealiased radial-velocity observations from PAR shifted to the sector volume scanned from 2008:46 to 2009:42 UTC.

APPENDIX B

Additional Dual-Doppler Analyses

a. Dual-Doppler analysis with the next PAR sector-volume scan

An additional dual-Doppler analysis is performed with the same dealiased radial-velocity observations from KTLX radar (scanned from 2004:28 to 2007:50 UTC) as for the dual-Doppler analysis in Fig. 6 but the dealiased radial-velocity observations from PAR are shifted to the next sector volume (scanned from 2006:17 to 2007:06 UTC). The analysis time window is the same as that for the dual-Doppler analysis in Fig. 6, but the analyzed VF can be considered about 2 min later than the analyzed VF in Fig. 6 because the PAR observations used here were scanned about 2 min later than those used for Fig. 6 in section 5. During this 2 min, the vortex center axis is advected about 1 km east-northeastward, as shown in Fig. B1.

The analyzed ($\mathbf{u}'$, w') fields are shown at z' = 1, 2, 3, and 4 km in the four panels of Fig. B2. As shown, the main gross structure of this VF is largely and roughly the same as that in Fig. 6 but its detailed fine structures and related intensities are changed from those in Fig. 6 especially for the w' field in and around the vortex core. These detailed changes indicate that transient fine structure variations in the true VF were too rapid to resolve by the dual-Doppler analyses (even with a temporal resolution of 2 min within the analysis time window).

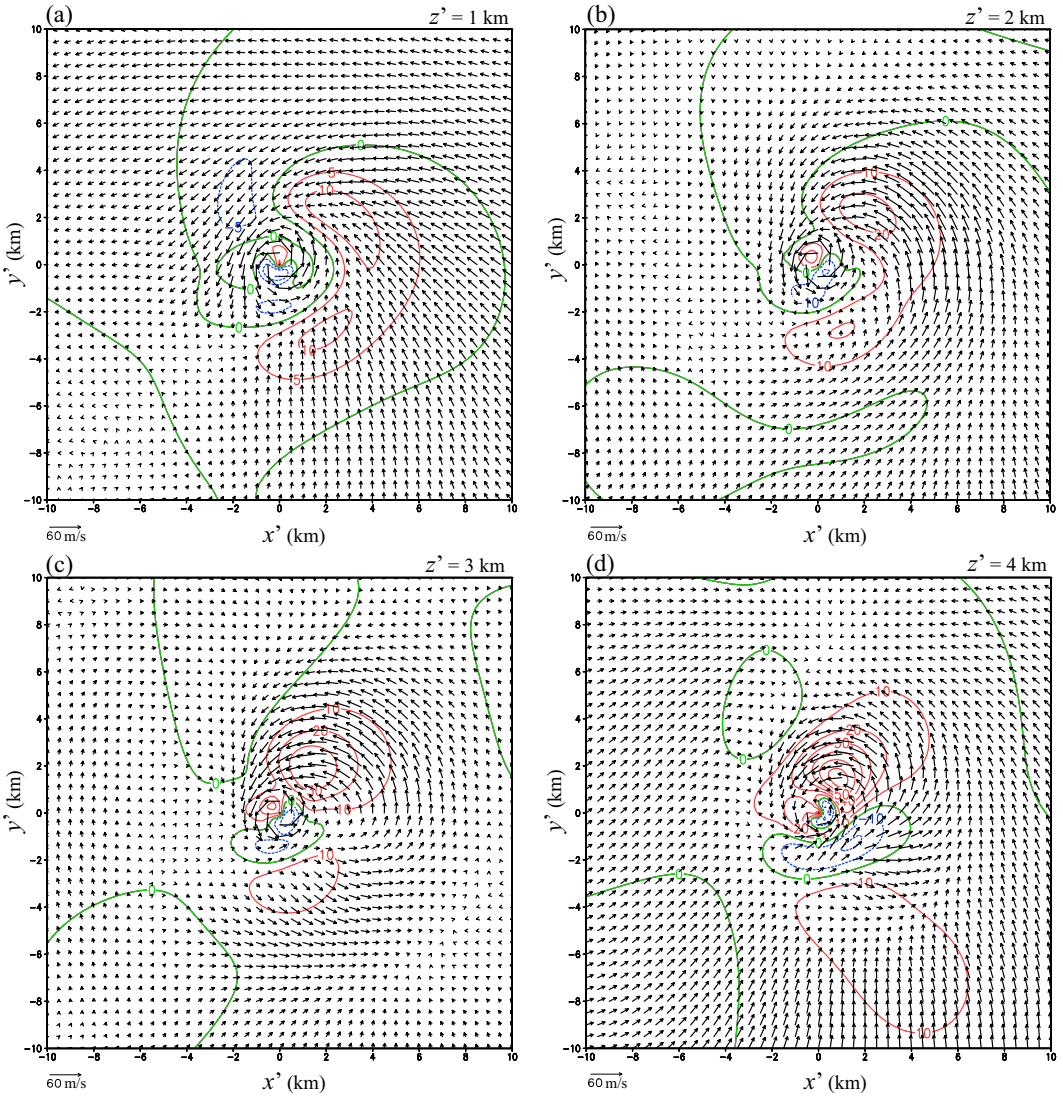

FIG. B4. As in Fig. B3, but for dual-Doppler-analyzed ($\mathbf{u}'$, w') obtained with the dealiased radial-velocity observations from KTLX radar further shifted by two more volumes to the volume scanned from 2017:15 to 2020:10 UTC and the dealiased radial-velocity observations from PAR further shifted to the sector volume scanned from 2017:28 to 2018:17 UTC.

b. Dual-Doppler analysis with the next KTLX volume scan

Another additional dual-Doppler analysis is performed with the radial-velocity observations from KTLX radar shifted to the next volume (scanned from 2008:42 to 2012:22 UTC) and the dealiased radial-velocity observations from PAR shifted to the sector volume scanned from 2008:46 to 2009:42 UTC. The analysis time window is still 4 min but from 2008:22 to 2012:22 UTC, so this time window is shifted forward by nearly 5 min from that for the dual-Doppler analyses in Figs. 6 and B2. During this 5 min, the vortex center axis is advected about 2 km east-northeastward and becomes less slanted but more curved, as shown in Fig. B1.

The analyzed ($\mathbf{u}'$, w') fields are shown at $z' = 1$, 2, 3, and 4 km in the four panels of Fig. B3. As shown, the main gross structure of this VF is changed slightly from that in Fig. B2 but its detailed fine structures and related intensities are changed significantly from those in Fig. B2 especially for the w' field in and around the vortex core and the $\mathbf{u}'$ field at $z' = 4$ km around the vortex core. These results indicate that the main structure of the true VF changed gradually but the fine structures of vortex winds especially vertical motions in and near the vortex core changed significantly as the time elapsed by 5 min.

c. Dual-Doppler analysis with the fourth subsequent KTLX volume scan

This third additional dual-Doppler analysis is performed with the dealiased radial velocities from KTLX radar further shifted by two more volumes to the volume scanned

from 2017:15 to 2020:10 UTC and the dealiased radial-velocity observations from PAR further shifted to the sector volume scanned from 2017:28 to 2018:17 UTC. The analysis time window is now shifted forward by nearly 9 min from that for the dual-Doppler analysis in Fig. B3. During this 9 min, the vortex center axis is advected about 5 km east-northeastward with its shape and slant direction changed from curved northward to highly curved southeastward, as shown in Fig. B1. In this case, the analysis domain is moved about 7 km east-northeastward in about 14 min from the location shown in Fig. 1, so observations from KTLX radar (or PAR) become scarce (or absent) for $z' \geq 4$ km in the moved analysis domain (as perceived by moving the analysis domain 7 km toward the KTLX radar site in Fig. 1 and Fig. 4).

The analyzed ($\mathbf{u}'$, w') fields are shown at $z' = 1$, 2, 3, and 4 km in the four panels of Fig. B4. As shown, the main gross structure of this VF is changed significantly from that in Fig. B3 especially for the w' field, and its detailed fine structures and related intensities are also changed substantially from those in Fig. B3 especially for the w' field in and around the vortex core and the $\mathbf{u}'$ field at $z' = 3$ and 4 km around the vortex core [although the analyzed ($\mathbf{u}'$, w') fields at $z' = 4$ km in Fig. B4d are likely subject to relatively large errors due to the shortage (or lack) of observation from KTLX radar (or PAR) as explained earlier]. These results indicate that the main structure of the true VF changed significantly as the time further elapsed by 9 min.

REFERENCES

Burgess, D., and Coauthors, 2014: 20 May 2013 Moore, Oklahoma, tornado: Damage survey and analysis. *Wea. Forecasting*, **29**, 1229–1237, https://doi.org/10.1175/WAF-D-14-00039.1.

Daley, R., 1991: *Atmospheric Data Analysis*. Cambridge University Press, 457 pp.

Davies-Jones, R., 1986: Tornado dynamics. *Thunderstorm Morphology and Dynamics*, E. Kessler, Ed., University of Oklahoma Press, 197–236.

——, R. J. Trapp, and H. B. Bluestein, 2001: Tornadoes and tornadic storms. *Severe Convective Storms*, *Meteor. Monogr.*, No. 50, Amer. Meteor. Soc., 167–222.

Fiedler, B. H., and G. S. Garfield, 2010: Axisymmetric tornado simulations with various turbulence models. *Comput. Fluid Dyn. Lett.*, **2**, 112–122.

Gao, J., and Coauthors, 2013: A real-time weather-adaptive 3DVAR analysis system for severe weather detections and warnings. *Wea. Forecasting*, **28**, 727–745, https://doi.org/10.1175/WAF-D-12-00093.1.

Heinselman, P., and S. Torres, 2011: High-temporal resolution capabilities of the National Weather Radar Testbed phased-array radar. *J. Appl. Meteor. Climatol.*, **50**, 579–593, https://doi.org/10.1175/2010JAMC2588.1.

Kurdzo, J. M., and Coauthors, 2017: Observations of severe local storms and tornadoes with the Atmospheric Imaging Radar. *Bull. Amer. Meteor. Soc.*, **98**, 915–935, https://doi.org/10.1175/BAMS-D-15-00266.1.

Lee, W. C., and J. Wurman, 2005: Diagnosed three-dimensional axisymmetric structure of the Mulhall tornado on 3 May 1999. *J. Atmos. Sci.*, **62**, 2373–2393, https://doi.org/10.1175/JAS3489.1.

Potvin, C. K., A. Shapiro, M. I. Biggerstaff, and J. M. Wurman, 2011: The VDAC technique: A variational method for detecting and characterizing convective vortices in multiple-Doppler radar data. *Mon. Wea. Rev.*, **139**, 2593–2613, https://doi.org/10.1175/2011MWR3638.1.

Snook, N., M. Xue, and Y. Jung, 2019: Tornado-resolving ensemble and probabilistic predictions of the 20 May 2013 Newcastle–Moore EF5 tornado. *Mon. Wea. Rev.*, **147**, 1215–1235, https://doi.org/10.1175/MWR-D-18-0236.1.

Wood, V. T., and R. A. Brown, 2011: Simulated tornadic vortex signatures of tornado-like vortices having one- and two-celled structures. *J. Appl. Meteor. Climatol.*, **50**, 2338–2342, https://doi.org/10.1175/JAMC-D-11-0118.1.

Xu, Q., 2021: A variational method for analyzing vortex flows in radar scanned tornadic mesocyclones. Part I: Formulations and theoretical considerations. *J. Atmos. Sci.*, **78**, 825–841, https://doi.org/10.1175/JAS-D-20-0158.1.

——, and K. Nai, 2017: Mesocyclone-targeted Doppler velocity dealiasing. *J. Atmos. Oceanic Technol.*, **34**, 841–853, https://doi.org/10.1175/JTECH-D-16-0170.1.

——, and L. Wei, 2021: A variational method for analyzing vortex flows in radar-scanned tornadic mesocyclones. Part II: Tests with analytically formulated vortices. *J. Atmos. Sci.*, **78**, 843–861, https://doi.org/10.1175/JAS-D-20-0159.1.

——, and ——, 2022: A variational method for analyzing vortex flows in radar-scanned tornadic mesocyclones. Part III: Sensitivities to vortex center location errors. *J. Atmos. Sci.*, **79**, 1515–1530, https://doi.org/10.1175/JAS-D-21-0203.1.

——, K. Nai, and L. Wei, 2007a: An innovation method for estimating radar radial-velocity observation error and background wind error covariances. *Quart. J. Roy. Meteor. Soc.*, **133**, 407–415, https://doi.org/10.1002/qj.21.

——, ——, ——, H. Lu, P. Zhang, S. Liu, and D. Parrish, 2007b: Estimating radar wind observation error and NCEP WRF background wind error covariances from radar radial-velocity innovations. *18th Conf. on Numerical Weather Prediction*, Park City, UT, Amer. Meteor. Soc., 1B.3, https://ams.confex.com/ams/22WAF18NWP/techprogram/paper_123419.htm.

——, L. Wei, W. Gu, J. Gong, and Q. Zhao, 2010: A 3.5-dimensional variational method for Doppler radar data assimilation and its application to phased-array radar observations. *Adv. Meteor.*, **2010**, 797265, https://doi.org/10.1155/2010/797265.

——, ——, K. Nai, S. Liu, R. M. Rabin, and Q. Zhao, 2015a: A radar wind analysis system for nowcast applications. *Adv. Meteor.*, **2015**, 264515, https://doi.org/10.1155/2015/264515.

——, ——, and ——, 2015b: Analyzing vortex winds in radar observed tornadic mesocyclones for nowcast applications. *Wea. Forecasting*, **30**, 1140–1157, https://doi.org/10.1175/WAF-D-15-0046.1.

——, ——, and ——, 2017: A three-step method for estimating vortex center locations in four-dimensional space from radar observed tornadic mesocyclones. *J. Atmos. Oceanic Technol.*, **34**, 2275–2281, https://doi.org/10.1175/JTECH-D-17-0123.1.

Xue, M., M. Hu, and A. D. Schenkman, 2014: Numerical prediction of the 8 May 2003 Oklahoma City tornadic supercell and embedded tornado using ARPS with the assimilation of WSR-88D data. *Wea. Forecasting*, **29**, 39–62, https://doi.org/10.1175/WAF-D-13-00029.1.

Zrnić, D. S., and Coauthors, 2007: Agile-beam phased array radar for weather observations. *Bull. Amer. Meteor. Soc.*, **88**, 1753–1766, https://doi.org/10.1175/BAMS-88-11-1753.